2011-09-01

Tev And Multi-Wavelength Observations Of Mrk 421 In 2006-2008

P. T. Reynolds
Cork Institute of Technology

Et. al.

The Astrophysical Journal, 738:25 (19pp), 2011 September 1 doi:10.1088/0004-637X/738/1/25

TeV AND MULTI-WAVELENGTH OBSERVATIONS OF Mrk 421 IN 2006–2008

V. A. Acciari[1], E. Aliu[2], T. Arlen[3], T. Aune[4], M. Beilicke[5], W. Benbow[1], D. Boltuch[6], S. M. Bradbury[7], J. H. Buckley[5], V. Bugaev[5], K. Byrum[8], A. Cannon[9], A. Cesarini[10], L. Ciupik[11], W. Cui[12], R. Dickherber[5], C. Duke[13], A. Falcone[14], J. P. Finley[12], G. Finnegan[15], L. Fortson[11], A. Furniss[4], N. Galante[1], D. Gall[19], G. H. Gillanders[10], S. Godambe[15], J. Grube[11], R. Guenette[16], G. Gyuk[11], D. Hanna[16], J. Holder[6], C. M. Hui[15], T. B. Humensky[17], A. Imran[18], P. Kaaret[19], N. Karlsson[11], M. Kertzman[20], D. Kieda[15], A. Konopelko[21], H. Krawczynski[5], F. Krennrich[18], M. J. Lang[10], G. Maier[16,35], S. McArthur[5], M. McCutcheon[16], P. Moriarty[22], R. A. Ong[3], A. N. Otte[4], M. Ouellette[23], D. Pandel[19], J. S. Perkins[1], A. Pichel[24], M. Pohl[18,35,36], J. Quinn[9], K. Ragan[16], L. C. Reyes[25], P. T. Reynolds[26], E. Roache[1], H. J. Rose[7], A. C. Rovero[24], M. Schroedter[18], G. H. Sembroski[12], G. Demet Senturk[27], D. Steele[11,37], S. P. Swordy[17,34], M. Theiling[1], S. Thibadeau[5], A. Varlotta[12], V. V. Vassiliev[3], S. Vincent[15], R. G. Wagner[8], S. P. Wakely[17], J. E. Ward[9], T. C. Weekes[1], A. Weinstein[3], T. Weisgarber[17], D. A. Williams[4], S. Wissel[17], M. Wood[3], B. Zitzer[12], A. Garson III[5], K. Lee[5], —BRT/NMS: A. C. Sadun[28], —Bell: M. Carini[29], D. Barnaby[29], K. Cook[29], J. Maune[29], A. Pease[29], S. Smith[29], R. Walters[29], —Tuorla/KVA: A. Berdyugin[30], E. Lindfors[30], K. Nilsson[30], M. Pasanen[30], J. Sainio[30], A. Sillanpaa[30], L. O. Takalo[30], C. Villforth[30], —WIYN: T. Montaruli[31], M. Baker[31], —Metsähovi: A. Lahteenmaki[32], M. Tornikoski[32], T. Hovatta[32], E. Nieppola[32], —UMRAO: H. D. Aller[33], and M. F. Aller[33]

[1] Fred Lawrence Whipple Observatory, Harvard-Smithsonian Center for Astrophysics, Amado, AZ 85645, USA
[2] Department of Physics and Astronomy, Barnard College, Columbia University, NY 10027, USA
[3] Department of Physics and Astronomy, University of California, Los Angeles, CA 90095, USA
[4] Santa Cruz Institute for Particle Physics and Department of Physics, University of California, Santa Cruz, CA 95064, USA
[5] Department of Physics, Washington University, St. Louis, MO 63130, USA; beilicke@physics.wustl.edu
[6] Department of Physics and Astronomy and the Bartol Research Institute, University of Delaware, Newark, DE 19716, USA
[7] School of Physics and Astronomy, University of Leeds, Leeds LS2 9JT, UK
[8] Argonne National Laboratory, 9700 S. Cass Avenue, Argonne, IL 60439, USA
[9] School of Physics, University College Dublin, Belfield, Dublin 4, Ireland
[10] School of Physics, National University of Ireland Galway, University Road, Galway, Ireland
[11] Astronomy Department, Adler Planetarium and Astronomy Museum, Chicago, IL 60605, USA
[12] Department of Physics, Purdue University, West Lafayette, IN 47907, USA
[13] Department of Physics, Grinnell College, Grinnell, IA 50112-1690, USA
[14] Department of Astronomy and Astrophysics, 525 Davey Lab, Pennsylvania State University, University Park, PA 16802, USA
[15] Department of Physics and Astronomy, University of Utah, Salt Lake City, UT 84112, USA
[16] Physics Department, McGill University, Montreal, QC H3A 2T8, Canada
[17] Enrico Fermi Institute, University of Chicago, Chicago, IL 60637, USA
[18] Department of Physics and Astronomy, Iowa State University, Ames, IA 50011, USA
[19] Department of Physics and Astronomy, University of Iowa, Van Allen Hall, Iowa City, IA 52242, USA
[20] Department of Physics and Astronomy, DePauw University, Greencastle, IN 46135-0037, USA
[21] Department of Physics, Pittsburg State University, 1701 South Broadway, Pittsburg, KS 66762, USA
[22] Department of Life and Physical Sciences, Galway-Mayo Institute of Technology, Dublin Road, Galway, Ireland
[23] Physics Department, California Polytechnic State University, San Luis Obispo, CA 94307, USA
[24] Instituto de Astronomia y Fisica del Espacio, Casilla de Correo 67-Sucursal 28, (C1428ZAA) Ciudad Autnoma de Buenos Aires, Argentina
[25] Kavli Institute for Cosmological Physics, University of Chicago, Chicago, IL 60637, USA
[26] Department of Applied Physics and Instrumentation, Cork Institute of Technology, Bishopstown, Cork, Ireland
[27] Columbia Astrophysics Laboratory, Columbia University, New York, NY 10027, USA
[28] Department of Physics, University of Colorado, Denver, CO 80217-3364, USA
[29] Department of Physics and Astronomy, Western Kentucky University, 1906 College Heights Blvd, Bowling Green, KY 42103, USA
[30] Tuorla Observatory, Department of Physics and Astronomy, University of Turku, Finland
[31] Physics Department, University of Wisconsin-Madison, Madison, WI 53706, USA
[32] Aalto University Metsähovi Radio Observatory, Metsähovintie 114, FIN-02540 Kylmala, Finland
[33] Department of Astronomy, University of Michigan, Ann Arbor, MI 48109-1042, USA
Received 2010 June 8; accepted 2011 June 6; published 2011 August 10

ABSTRACT

We report on TeV γ-ray observations of the blazar Mrk 421 (redshift of 0.031) with the VERITAS observatory and the Whipple 10 m Cherenkov telescope. The excellent sensitivity of VERITAS allowed us to sample the TeV γ-ray fluxes and energy spectra with unprecedented accuracy where Mrk 421 was detected in each of the pointings. A total of 47.3 hr of VERITAS and 96 hr of Whipple 10 m data were acquired between 2006 January and 2008 June. We present the results of a study of the TeV γ-ray energy spectra as a function of time and for different flux levels. On 2008 May 2 and 3, bright TeV γ-ray flares were detected with fluxes reaching the level of 10 Crab. The TeV γ-ray data were complemented with radio, optical, and X-ray observations, with flux variability found in all bands except for the radio wave band. The combination of the *Rossi X-ray Timing Explorer* and *Swift* X-ray data reveal spectral hardening with increasing flux levels, often correlated with an increase of the source activity in TeV

γ-rays. Contemporaneous spectral energy distributions were generated for 18 nights, each of which are reasonably described by a one-zone synchrotron self-Compton model.

Key words: BL Lacertae objects: individual (Mrk 421) – galaxies: jets – galaxies: nuclei – gamma rays: galaxies – X-rays: galaxies

Online-only material: color figures

1. INTRODUCTION

In 1992, observations with the Whipple 10 m Cherenkov telescope led to the first discovery of an extragalactic source of TeV γ-rays, the blazar Mrk 421 (Punch et al. 1992). Since then, more than 30 similar sources have been detected with ground-based γ-ray detectors (Wakely & Horan 2010). The sources with well-measured redshifts lie from 0.031 (Mrk 421; Snellen et al. 2002) to 0.536 for the recently detected radio quasar 3C 279 (Albert et al. 2008). Typically, blazars show core-dominated emission, and they are characterized by rapid variability. Their spectral energy distribution (SED) in the νF_ν representation is characterized by two broad, well-separated "humps" arising from (1) synchrotron emission (low energy) and (2) a high-energy component of either leptonic or hadronic nature. During TeV γ-ray flares, strong sources (i.e., Mrk 421 and PKS 2155-304) exhibit νF_ν-fluxes of about 10^{-9} erg cm^{-2} s^{-1} (Aharonian et al. 2009b), corresponding to γ-ray luminosities between 10^{42} and 10^{43} erg s^{-1} for assumed anisotropic emission with an opening angle of 5 deg. The blazars detected at TeV energies are the high-frequency peaked counterparts of the blazar source population detected at MeV/GeV energies with the EGRET experiment on board the space-borne *Compton Gamma Ray Observatory* (Hartman et al. 1999), and recently expanded by the Large Area Telescope (LAT) on board the *Fermi* γ-ray satellite (Abdo et al. 2010).

Following the detection in TeV γ-rays in 1992, Mrk 421 was observed intensively, and the observations led to a number of landmark discoveries.

1. The detection of fast flux variability with a doubling time of 15 minutes (Gaidos et al. 1996).
2. The first tentative evidence for an X-ray/TeV γ-ray flux correlation (Buckley et al. 1996). Several observation campaigns strengthened the evidence for such a correlation. Some of the most convincing results were presented by Fossati et al. (2008).
3. The detection of TeV γ-ray energy spectra that harden with increasing fluxes (Krennrich et al. 2002).

Modeling of Mrk 421 data with synchrotron-Compton models revealed the first evidence for bulk jet Lorentz factors of the order of 50 (Krawczynski et al. 2001) and modeling of data taken during different states revealed evidence that one-zone synchrotron self-Compton (SSC) models are insufficient to describe the observations (Błażejowski et al. 2005). Alternative models are discussed in the literature. Recent papers include Katarzyński & Walczewska (2010), Böttcher & Dermer (2010), Gao et al. (2010), Tammi & Duffy (2009), Lichti et al. (2008), and Stecker et al. (2007). These models involve more complicated geometries which lead to a larger number of free model parameters than in the SSC model.

Mrk 421 has been a frequent target of multi-wavelength (MWL) campaigns. During some of its very short flares the X-ray and TeV γ-ray fluxes tracked each other (Fossati et al. 2008). However, X-ray flares that are not accompanied by TeV γ-ray flares and vice versa have also been observed (Rebillot et al. 2006; Fossati et al. 2008). There is good evidence that the X-ray and TeV γ-ray activities are correlated when averaged over $\sim$1 week time intervals (Błażejowski et al. 2005; Horan et al. 2009). All attempts to establish convincing evidence for a correlation of the X-ray and γ-ray fluxes with the flux variability at radio to optical wavelengths have failed so far (Błażejowski et al. 2005; Horan et al. 2009).

The X-ray/TeV γ-ray correlation properties are of great interest, as they might enable us to decide on the emission model, i.e., between (1) leptonic models in which a single population of high-energy electrons emits the low- and high-energy radiation as synchrotron and inverse Compton (IC) emission, respectively, and (2) hadronic models in which the γ-ray emission is attributed to additional population(s) of high-energy particles, powered by the acceleration of extremely high-energy protons. It is interesting to note that the X-ray/TeV γ-ray flux correlation has only been studied for a handful of sources (Mrk 421, Mrk 501, 1 ES1959+650, PKS 2155-305, and 1 ES2344+514) with a sufficiently good signal-to-noise ratio in both bands to investigate the correlation properties. Although the X-ray and TeV γ-ray fluxes seem to be correlated, it is not clear how well this correlation holds for individual flares (Krawczynski et al. 2004).

In this paper, we report on the first TeV γ-ray observation campaign on Mrk 421 performed with the VERITAS observatory. VERITAS achieves an energy flux sensitivity of $(t_{\rm obs}/50\,{\rm hr})^{-1/2} \times 5 \times 10^{-13}$ erg cm^{-2} s^{-1} at 500 GeV.[38] The high sensitivity of VERITAS and the brightness of Mrk 421 during flares allow us to measure fluxes with $\sim$minute time bins and to determine energy spectra for 5 minute time intervals or less. We also report accompanying observations in the radio band, at optical wavelengths, and in the X-ray band with the *Rossi X-ray Timing Explorer* (*RXTE*) Proportional Counter Array (PCA), *Swift* X-ray telescope (XRT), and *Suzaku* instruments.

In Section 2, we discuss the data sets and the analysis methods. The results of different studies are presented in Section 3 followed by a summary and discussion in Section 4.

2. DATA SETS AND DATA REDUCTION

In this section, we describe the observations and analysis of the data taken in the TeV energy regime (Section 2.1), at X-ray

[34] Deceased.
[35] Now at DESY, Platanenallee 6, 15738 Zeuthen, Germany.
[36] Now at Institut für Physik und Astronomie, Universität Potsdam, 14476 Potsdam-Golm, Germany.
[37] Now at Los Alamos National Laboratory, MS H803, Los Alamos, NM 87545, USA.

[38] In terms of the flux from the Crab Nebula, the VERITAS sensitivity is $(t_{\rm obs}/30\,{\rm minute})^{-1/2} \times 8\%$ Crab in 30 minutes of observations. This number is valid for the VERITAS array as operated in 2008.

energies (Section 2.2), as well as in the optical (Section 2.3) and radio (Section 2.4) wave bands.

2.1. VERITAS/Whipple γ-Ray Data

VERITAS. VERITAS[39] consists of four 12 m diameter imaging atmospheric Cherenkov telescopes and is located at the base camp of the Fred Lawrence Whipple Observatory (FLWO) in southern Arizona at an altitude of 1280 m. It detects the Cherenkov light emitted by an extensive air shower (initiated by a γ-ray photon or cosmic ray entering Earth's atmosphere) using a 499 pixel photomultiplier camera located in the focal plane of each telescope. The array is sensitive to γ-rays in the energy range from ~100 GeV to ~30 TeV. Observations are performed (in 20 minute runs) on moonless nights using the "wobble" mode of operation, where all telescopes are pointed to a sky position offset of ± 0.5 deg (alternating in direction between consecutive data runs) with respect to the source position. This method allows for a simultaneous background estimation to be made. More details about VERITAS, the data calibration, and the analysis techniques can be found in Acciari et al. (2008).

Only shower images which pass certain quality cuts are considered in the event reconstruction: image size $\geqslant$500 digital counts[40] (dc) and image distance to the center of the camera $<$1.43 deg. The standard cuts for γ/hadron separation, which are based on the width and length of the recorded images (Acciari et al. 2008), were a priori optimized on data taken from the Crab Nebula. An event is considered to fall into the signal (ON) region once the squared angular distance between the reconstructed event direction and the Mrk 421 position is $\Delta\theta^2 \leqslant 0.025$ deg^2. The background is estimated from different regions of the same size positioned at the same radial distance to the camera center as the ON region and is referred to as the reflected background region model (Berge et al. 2007). The excess is then calculated as the number of ON-source counts less the normalized number of OFF region counts. In this analysis five OFF regions were used. The statistical significances are calculated using the method of Li & Ma (1983).

The energy E_i of an individual image is estimated using look-up tables generated from Monte Carlo simulations of γ-ray air showers. The tables are parameterized in (1) the integrated charge (size), (2) the impact parameter p_i between the reconstructed shower axis and the optical axis of telescope i, (3) the zenith angle z, (4) the azimuth angle Az, and (5) the level of the night-sky background. The energy of the shower event is then averaged over the n telescope energies to obtain $E_{\rm reco} = 1/n \sum_{i=1}^{n} E_i$. The energy resolution is estimated based on Monte Carlo simulations to be $\Delta E/E \approx 20\%$ for energies between 100 GeV and 30 TeV.

The effective areas $A_{\rm eff}$ describe the energy-dependent response of the detector and are also obtained by Monte Carlo simulations. The effective area $A_{\rm eff}(E_{\rm reco}, z, Az, \Delta R, N_{\rm tel})$ is estimated for each event based on its corresponding parameters; ΔR is the angular distance between the reconstructed shower direction and the telescope pointing position, $N_{\rm tel}$ is the number of telescopes in the system.[41]

The inverse effective areas are used on an event-by-event basis to calculate the differential photon flux for each bin j in the energy spectrum:

$$\frac{dN}{dE_{\rm j}} = \frac{1}{T_j^{\rm live} \cdot \Delta E_j} \left(\sum_{k=1}^{N_{\rm on,j}} \frac{1}{A_{\rm eff,k}} - \alpha \sum_{k=1}^{N_{\rm off,j}} \frac{1}{A_{\rm eff,k}} \right). \quad (1)$$

The sum of $N_{\rm on}$ corresponds to reconstructed events from the ON region and the sum of $N_{\rm off}$ to events from the five reflected OFF regions with the normalization $\alpha = 0.2$. $T_j^{\rm live}$ is the live time for bin j. The bias energy describes the energy at which the reconstructed energy $E_{\rm reco}$ (on average) deviates less than a certain percentage from the true energy $E_{\rm MC}$. The energy bias is calculated based on Monte Carlo simulations; a bias threshold of $(E_{\rm reco} - E_{\rm MC})/E_{\rm MC} = 10\%$ is used in this analysis. The bias energy depends on the zenith angle of the corresponding data run. For each 20 minute run, the bias energy is calculated and only those bins, j, in the energy spectrum which are fully contained above the bias energy are allowed to receive events. The live time $T_j^{\rm live}$ is increased on a run-by-run basis for only those energy bins.

In order to account for spillover effects, the effective areas are calculated using the reconstructed energies, where the Monte Carlo input spectrum is weighted according to the reconstructed/measured spectrum in an iterative procedure. The systematic errors of the parameters describing a power-law energy spectrum $dN/dE = I_0 \cdot E^{-\Gamma}$ have been estimated[42] based on a Crab-like energy spectrum ($\Gamma \approx 2.5$) to be $\Delta\Gamma/\Gamma = 8\%$ and $\Delta I_0/I_0 = 20\%$.

The integral flux on a run-by-run basis above a certain energy E' (as shown in the light curves) is calculated as follows: a spectral slope is assumed and the effective areas for the corresponding run parameters (zenith angle, etc.) are used together with the measured excess to determine the normalization. The normalization is then used to calculate the integral flux above E'. This procedure has the advantage that the full event statistics are used and E' is not limited by the strongly varying thresholds of individual data subsets (i.e., runs taken at different zenith angles). However, a spectral shape has to be assumed, which in our case is chosen (iteratively) for each data point according to the energy spectrum corresponding to the estimated flux level.

Mrk 421 is one of the objects in a trigger agreement between the γ-ray observatories H.E.S.S., MAGIC, and VERITAS put into place for known TeV γ-ray blazars in order to exchange information about flaring sources. The trigger criterion for Mrk 421 is defined by a flux level measured by one of the observatories exceeding a value of $2\Phi_{\rm crab}$; this criterion was met several times during the campaign in 2008, leading to triggers sent by VERITAS and to triggers received from the MAGIC collaboration. VERITAS observed Mrk 421 during 2007 January/February and November/December (5 hr) as well as in 2008 January to June (42.3 hr) for a total of 47.3 hr after run quality selection. The observation time corrected for the detector dead time amounts to 43.6 hr. The zenith-angle range of the observations was 6–56 deg with an average of 23.5 deg, corresponding to an analysis energy threshold[43] of 260 GeV.

Whipple. The 10 m γ-ray Telescope at the FLWO (Kildea et al. 2007) is sensitive in the energy range from 200 GeV to 20 TeV with a peak response energy (for a Crab-like spectrum)

[39] Very Energetic Radiation Imaging Telescope Array System.

[40] The photomultiplier pulses are integrated within a time window of 24 ns duration. One photoelectron corresponds to approximately five digital counts.

[41] A part of the Mrk 421 data were taken with only $N_{\rm tel} = 3$ operating telescopes.

[42] Uncertainties in the atmosphere, components of the detector, and shower reconstruction algorithms were considered in this estimate.

[43] The energy threshold is defined as the energy corresponding to the peak detection rate for a Crab-like spectrum.

Table 1
Pointed X-ray Observations (*RXTE*/PCA, *Swift*/XRT, and *Suzaku*/XIS) of Mrk 421 in 2006 to 2008

Start	Stop	N_{obs}	ObsID
RXTE/PCA			
2006 Jan 6	2006 Mar 2	27	91440-01
2006 Mar 3	2006 May 31	48	92402-01
2008 Jan 7	2008 May 7	86	93133-02
Swift/XRT			
2006 Jan 2	2006 Dec 5	20	
2007 Mar 23	2007 Dec 31	24	
2008 Jan 7	2008 May 8	54	
Suzaku/XIS			
2008 May 5	2008 May 8	1	

of approximately 400 GeV. This telescope, although a factor of seven less sensitive than VERITAS, was used in this program to extend the TeV coverage when VERITAS was not available for Mrk 421 observations. More detailed descriptions of Whipple observing modes and analysis procedures can be found elsewhere (Weekes 1996; Punch & Fegan 1991; Reynolds et al. 1993). Details about the Whipple telescope including the GRANITE-III camera have been given in Kildea et al. (2007).

The Whipple observations were conducted between 2005 November and 2008 May (MJD 54417–54622). Only runs which pass the run quality selection (stability of the raw trigger rate, induced by the cosmic-ray background) are considered in the analysis resulting in a data set of 96 hr of ON-source data. The data were analyzed using the standard second-moment-parameterization technique (Hillas 1985). Standard cuts (`SuperCuts2000`) were used to select γ-ray events and to suppress background cosmic-ray events (de la Calle Perez et al. 2003). Using the zenith-angle dependence of a Crab data set taken at similar epochs, we account for the zenith-angle dependence of the γ-ray excess rate by normalizing our measured Mrk 421 rate to the Crab rate at a corresponding zenith angle. It should be noted that this simplistic scaling is strictly only valid for a TeV spectrum close to that of the Crab Nebula (spectral index of $\Gamma = 2.5$). However, the systematic error introduced by this scaling can be expected to be small compared to the statistical error of the flux points.

2.2. RXTE, SWIFT, and Suzaku X-Ray Observations

X-ray data were taken with the telescopes on the *RXTE* (Swank 1994), *Swift* (Gehrels et al. 2004), and *Suzaku* (Mitsuda et al. 2007) satellites. The pointed X-ray observations are summarized in Table 1.

RXTE/PCA. The PCA (Jahoda et al. 1996) comprises five Proportional Counter Units (PCUs) covering a nominal energy range of 2–60 keV with a net detection area of 6250 cm^2. Data between the energies of 3–15 keV were used in this analysis. The 15–250 keV data from the High-Energy X-ray Timing Experiment (Rothschild et al. 1998) were not used owing to an insufficient signal-to-noise ratio. The PCA data were taken as part of a MWL observation proposal and comprise 161 exposures between 2006 January and 2008 May (see Table 1) with a total net exposure time of 245.6 ks. The observations had a typical exposure of 10–70 minutes per pointing and were taken at near-simultaneous times to scheduled VERITAS observations.[44] For the observations from 2006 January 6 to 2006 April 18 both PCU0 and PCU2 detectors collected data, while for all other data only PCU2 was operational. The data were filtered following the standard criteria advised by the NASA Guest Observer Facility (GOF).[45] Standard-2 mode PCA data gathered with the top layer (X1L and X1R) of the operational PCUs were analyzed using the HEAsoft 6.4 package. Background models were generated with the tool *pcarsp*, based on the *RXTE* GOF calibration files for a "bright" source with more than 40 counts s^{-1}. Response matrices for the PCA data were created with the script *pcarsp*. The *saextrct* tool was used to extract all PCA energy spectra.

RXTE/ASM. The *RXTE* All Sky Monitor (ASM; Levine et al. 1996) is sensitive to X-ray energies at 2–12 keV and scans most of the sky every 1.5 hr. The data were obtained from the public MIT archive[46] in the form of 1 day averaged binning as well as the dwell-by-dwell binning (for the short-term light curve and flux correlation studies).

Swift/XRT. The XRT on board the *Swift* satellite (Gehrels et al. 2004) is a focusing XRT with a 110 cm^2 effective area and a 23′ field of view (Burrows et al. 2005). It is sensitive to X-rays in the 0.2–10 keV band. A total of 1175.7 ks of XRT data were taken between 2006 January and 2008 May (Table 1) in the Windowed Timing mode with grades 0–2 (referring to the pattern of CCD pixels for each event) selected over the energy range 0.4–10 keV. The XRTPIPELINE tool was used to calibrate and clean all *Swift* XRT event files with current calibration files. The data were reduced using the HEAsoft 6.4 package. Source counts were extracted from a rectangular region of 40 pixels (94.4 arcsec) along the one-dimensional stream and 20 pixels high centered on the source. Background counts were extracted from a nearby source-free rectangular region of equivalent size. Ancillary response files were generated using the *xrtmkarf* task applying corrections for the point-spread function losses and CCD defects. The latest response matrix from the XRT calibration files was used. The extracted XRT energy spectra were re-binned to contain a minimum of 20 counts in each bin and were fit with XSPEC 12.4.

Swift/BAT. The Burst Alert Telescope (BAT) is a large field of view (1.4 sr) XRT with imaging capabilities in the energy range from 15to150 keV (Gehrels et al. 2004). The BAT typically observes 50%–80% of the sky each day. The data are the *Swift*/BAT transient monitor results provided by the *Swift*/BAT team (Krimm 2008a). Full details of the BAT data analysis are given at the BAT transients Web site (Krimm 2008b).

Suzaku/XIS. The X-ray Imaging Spectrometer (XIS; Koyama et al. 2007) on board the *Suzaku* satellite is composed of three X-ray CCD cameras combined with a single XRT covering a nominal energy range of 0.5–12 keV. Each CCD camera covers an 18′ × 18′ region of the sky. The XIS data include observations between 2008 May 5 and May 8 with an exposure time of 180.8 ks. Standard data reduction and processing were performed using HEAsoft v6.6.3 and ftools v6.6. XIS events were extracted from a source region with an inner radius of 35 pixels and an outer radius of 408 pixels. The extent of the inner radius is such that pile-up effects were minimized for the selected events. The background was selected from an annulus outside of the source region defined by 432 pixel and 464 pixel

[44] The *RXTE*/PCA staff at NASA GSFC and Principal Investigator (PI) of the observation proposal Henric Krawczynski, together with the VERITAS team, coordinated the observations.
[45] http://heasarc.gsfc.nasa.gov/docs/xte/xte_1st.html
[46] http://heasarc.gsfc.nasa.gov/docs/xte/asm_products.html

inner and outer radii, respectively. The response matrix and effective area were calculated for each XIS sensor using the *Suzaku* ftools tasks, *xisrmfgen* and *xissimarfgen* (Ishisaki et al. 2007). XIS1 data were not included in this analysis. As the XIS0 and XIS3 have similar responses, their data were summed.

2.3. Optical Observations

Many optical observatories contributed data sets to this campaign (see below). The data from the observatories were reduced and the photometry performed independently by different analysts using different strategies. The same set of reference stars was used for all optical data sets to calculate the systematic error on the flux. However, combining the various optical data to produce a composite light curve for each spectral band is complicated by the fact that different observatories use different photometric systems. Furthermore, photometric apertures and the definition of the reported measurement error for each nightly averaged flux is inconsistent across data sets. Therefore, we have adopted a simple approach for the construction of the composite light curves whereby a unique flux offset is found for each spectral band (*R*, *B*, *V*) of every instrument based on overlapping observations (Steele et al. 2008), and the light curves have been scaled accordingly (in our case the light curves of the Bradford Robotic Telescope (BRT) and the New Mexico Skies (NMS) observatory by 15% each).

UVOT. Mrk 421 was observed with the *Swift* Ultraviolet/Optical Telescope (UVOT) during 2008. The instrument cycled through each of three ultraviolet pass bands, UVW1, UVM2, and UVW2 with central wavelengths of 260 nm, 220 nm, and 193 nm, respectively. More than 100 observations were obtained with a typical/average exposure (per filter) of 150 s, ranging from 50 s up to 900 s. Data were taken in the *image mode*, where the image is accumulated on board the satellite discarding the photon timing information within each single exposure to reduce the telemetry volume and the time of transmission.

Primary and secondary analyses were carried out using UVOTSOURCE standard tool and a custom UVOT pipeline. Both analyses used the calibration database released on 2010 February. Photometry was computed using a 5″ source region around the source and photometric corrections were applied following Poole et al. (2008) and Li et al. (2006). All observations were inspected manually. Astrometric misalignment between the observed position and the nominal position of Mrk 421 which were found in several data sets were corrected by using a spatial fitting algorithm. Results of the two analysis chains were found to be in agreement.

Due to the ultraviolet spectrum, we adopted the rate-to-flux conversion factors for gamma-ray-burst-like objects and not the standard factors used for Pickles-like star spectra. The fluxes were corrected for galactic extinction $E_{B-V} = 0.015$ mag (Schlegel et al. 1998). To obtain this value we smoothed the nearer values of the database in correspondence with the coordinates of the source. Then, the computed optical/UV galactic extinction coefficients were applied (Fitzpatrick & Massa 1999). The effects of intergalactic absorption and the zodiacal light have been estimated to be negligible and were not corrected for in this analysis. The fluxes and corresponding frequencies shown in the light curves are redshift corrected, including a second-order correction taking into account filter nonlinearities.

The host galaxy correction was not applied, but a systematic error on the flux is estimated. The measurements of Nilsson et al. (1999) are used to estimate the host galaxy emission in the *R* band. These are used to obtain the corresponding components for the *V*, *B*, and *U* bands (Fukugita et al. 1995). The presence of an upturn flux excess in the far UV spectrum of elliptical galaxies is caused by an old population of hot helium-burning stars without extended hydrogen-rich envelopes (as compared to rather young stars). The findings of Arimoto (1996) were used to calculate the metallicity of the Mrk 421 host galaxy and therefore constrain its contribution to the UV bands to be less than 5% (Han et al. 2007).

Some caveats have to be mentioned. There are bright sources in the field of view which will cause significant coincidence losses, ghosting from internal reflections, and may lead to an additional overestimation of the Mrk 421 blazar flux. Although the relative photometry (light curves) is expected to be less sensitive to these effects, an additional systematic error of 20% was added to the absolute UVOT fluxes shown in the SEDs to account for these uncertainties.

BRT/NMS. Optical data were taken with the BRT in Tenerife, Canary Islands, Spain as well as the NMS observatory (NMS). The data were reduced by standard aperture photometry.[47] The aperture size used was 10″ diameter, and the comparison stars were taken from Villata et al. (1998).

Bell. The Western Kentucky University's Bell observatory is a 0.6 m telescope located 12 miles southwest of Bowling Green, Kentucky. The observations presented here were obtained with an AP6 CCD camera and Bessell *R*-band filter. Dark and flat-field corrections were made to the images, and differential aperture CCD photometry was performed using stars 1,3,2 of the comparison sequence from Villata et al. (1998). No correction for host galaxy flux or galactic absorption was made.

WIYN. The WIYN 0.9m telescope is located at the National Optical Astronomy Observatory at Kitt Peak and operated by a consortium of universities. Observations of Mrk 421 were performed since 2006 January in Johnson *B* and *V* and Cousins *R* optical filters and a CCD 1 deg field of view Mosaic Imager. Image reduction was performed with IRAF, using bias frames and dome flat fields for each night of data. We obtained magnitudes by differential photometry, using three reference stars from Villata et al. (1998). Since we are mostly interested in measuring the magnitude relative variations with time, these data were not corrected for the host galaxy flux or absorption.

Tuorla/KVA. The Kungliga Vetenskapsaka-demien telescope (KVA; Royal Swedish Academy of Sciences) is located on Roque de los Muchachos, La Palma and operated by the Tuorla Observatory, Finland. The telescope is composed of a 0.6 m f/15 Cassegrain devoted to polarimetry, and a 0.35 m f/11 Schmidt–Cassegrain Telescope auxiliary telescope for multicolor photometry. This telescope has been successfully operated in a remote way since autumn 2003. Mrk 421 has been observed in optical *R* band typically once per night. Photometric measurements were made in differential mode, i.e., by obtaining CCD images of the target and calibrated comparison stars in the same field of view (Fiorucci & Tosti 1996; Fiorucci et al. 1998; Villata et al. 1998).

2.4. Radio Observations

Radio data presented here were taken at four frequencies at two different radio observatories. The fluxes are given in Janskys (Jy), so they have already been normalized for the bandwidth of their receivers.

[47] The MIRA Pro Version 7 (Mirametrics, Inc.) was used, see http://www.mirametrics.com/.

Metsähovi. The Metsähovi radio telescope (radome enclosed paraboloid antenna, diameter of 13.7 m) is situated in Finland. The measurements were made with a 1 GHz band dual beam receiver centered at 36.8 GHz. The observations are ON–ON observations (typical integration time of 1200–1400 s), alternating the source and the sky in each feed horn.

The detection limit of the telescope at 37 GHz is of the order of 0.2 Jy under optimal conditions. Data points with a signal-to-noise ratio <4 are handled as non-detections. The flux density scale is set by observations of DR 21. Sources 3C 84 and 3C274 are used as secondary calibrators. A detailed description of the data reduction and analysis is given in Teräsranta et al. (1998). The error estimate in the flux density includes the contribution from the measurement rms and the uncertainty of the absolute calibration.

UMRAO. The University of Michigan Radio Astronomy Observatory (UMRAO) (26 m paraboloid) provided monitoring data of Mrk 421 at 4.8 GHz, 8 GHz, and 14.5 GHz between 2006 June and 2008 May. Each observation consisted of a series of ON–OFF measurements taken over a 30–40 minute time period. All observations were made within a total hour angle range of about 5 hr centered on the meridian. The calibration and reduction procedures have been described in Aller et al. (1985). Some daily observations were averaged to improve the signal-to-noise ratio.

Unfortunately, the source is rather weak which may mask some variability. Nevertheless, the UMRAO measurements over many decades have identified continuous fluctuations in amplitude but not a single outburst-like flare. Small structural changes in the radio jet are apparent in the MOJAVE 15 GHz very long baseline interferometry images for the source.[48]

3. RESULTS

In the whole VERITAS data set an excess of 29974 γ-ray events was detected from the direction of Mrk 421 after application of event selection cuts (31523 ON events, 7746 OFF events, normalization $\alpha = 0.2$), corresponding to a statistical significance of 277 standard deviations. An overview of the light curves at radio to TeV energies is given in Section 3.1. Subsequently, we discuss the time and spectral variability of the TeV γ-ray data (Section 3.2) as well as the time and spectral variability of the X-ray fluxes (Section 3.3) on different timescales. Finally, we scrutinize how those relate to the flux and spectral variability in other energy bands in Section 3.4.

3.1. Light Curves

The radio, optical, X-ray, and TeV light curves of Mrk 421 are shown in Figure 1 for the years 2006–2008 during which the source was extensively monitored in the various energy bands. A zoomed version for the year 2008 is shown in Figure 2. Two further levels of zoom are shown in Figures 3 (the two more active X-ray/TeV states) and 4 (the strong TeV γ-ray flare).

For a clearer representation, the *RXTE*/ASM and *Swift*/BAT night-by-night data points in Figures 1–3 were combined until one of the following conditions was met: (1) the combined data point had a statistical significance of more than three standard deviations (σ) or (2) 15 bins of the original light curve were combined. The *RXTE*/ASM and *Swift*/BAT data in Figure 4 are shown in dwell-by-dwell bins. The TeV data (Whipple and VERITAS) in all figures are shown in a run-by-run binning of 10–20 minute duration. All other data are shown in a binning corresponding to the pointings/exposures of the individual experiments.

Although the X-ray fluxes show a long-term structure with phases of higher activity followed by phases of lower activity, flux variations by a factor of two can be observed on timescales down to a few days. In the optical band, flux variations are observed on longer timescales of the order of weeks to months. The structure of the optical light curve (i.e., Figure 2) and possible connections to the X-ray/TeV band are discussed in Section 3.4. No significant flux variations can be observed at radio energies. The flux correlations between the different energy bands are discussed in Section 3.4. Two phases of enhanced X-ray and/or TeV activity can be identified in the light curve.

1. *Phase 1:* The first active phase (*phase 1*) occurred during the summer 2006 and lasted for at least a few months. The active state can be identified in soft and hard X-rays (Figure 1). During this time period no VERITAS data were taken and only a few nights are covered by Whipple data.
2. *Phase 2:* The second active phase (*phase 2*) occurred in 2008 April/May and was recorded with excellent coverage in the X-ray and TeV bands (Figure 2). However, a zoom-in of this second flaring phase (Figures 3 and 4) shows that the strongest TeV emission (*phase 2b*) is not coincident with the strongest soft/hard X-ray activity (*phase 2a*, peaking roughly one month before phase 2b). The lack of increased X-ray emission during the peak TeV flaring might indicate an orphan flare (Krawczynski et al. 2004). However, the characteristic timescales of flux changes in the TeV band can be less than an hour (the major flare is fully contained within a time interval of 5 hr), so that a detailed comparison has to be restricted to closely simultaneous data, see Section 3.4. The TeV flare is followed by a somewhat enhanced X-ray flux: the *Swift*/BAT, *Swift*/XRT, and *RXTE*/PCA data indicate a doubling in flux level between the night of the flare and the following night, declining back to the previous level within a few days, which is nicely sampled by the *Suzaku*/XIS (Figure 4). The corresponding structure of the X-ray light curve, however, does not substantially differ from low-state variations, so that a physical connection to the TeV activity cannot be claimed.

3.2. Temporal and Spectral Variability in the TeV γ-Ray Band

Flux variability. Flux variations on timescales of 1–2 days are found in the TeV band. Except for two nights measured during a strong flare in 2008 May (phase 2b, Figure 3), no significant TeV flux variations are observed within individual nights. It should, however, be mentioned that the observation time during individual nights often did not exceed 10–20 minutes.[49] This prevents placing strong constraints on the $\gtrsim$0.5–1 hr timescale variability, given the low/medium states of Mrk 421 during most of the measurements. Nevertheless, the strong outburst measured in 2008 May (Figure 4) clearly shows variability on sub-hour timescales even though the flare was recorded at zenith angles down to 60 deg (see insets in Figure 4). At high zenith angles z, the effective areas vary drastically with a small change in z and the sensitivity suffers from the strongly increased energy threshold (leading to a huge loss in event statistics). Since the data points in the light curve are given above 300 GeV, the

[48] Mrk 421 on the MOJAVE (monitoring of jets in active galactic nuclei with VLBA experiments) project page: http://www.physics.purdue.edu/astro/MOJAVE/sourcepages/1101+384.shtml

[49] Regular run durations are 20 minutes, but for monitoring purposes, some observations were conducted with just 10 minutes per night.

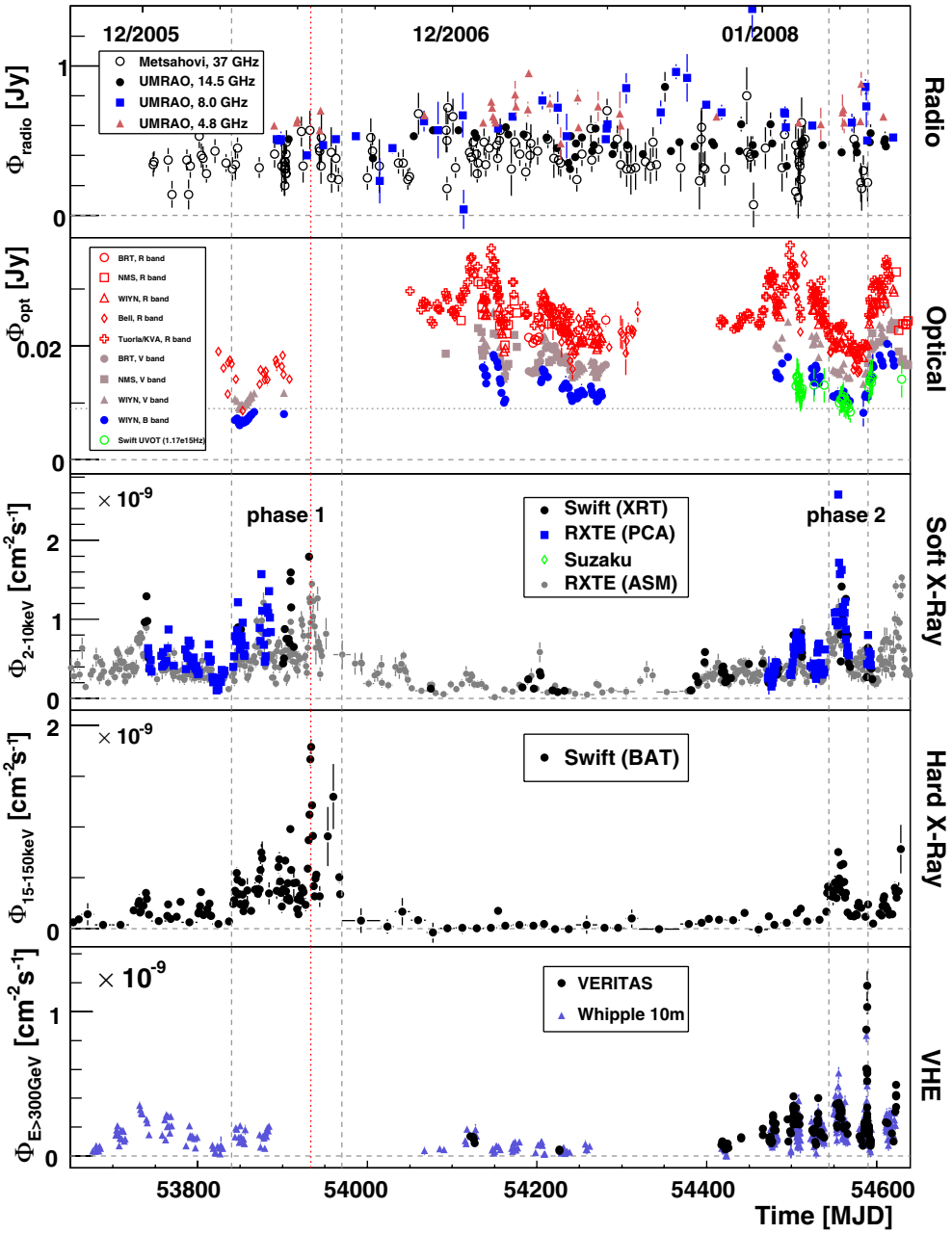

Figure 1. Mrk 421 light curves measured by different experiments (see Section 2) in 2006–2008. All errors are statistical errors only. Shown are the radio band (upper panel), the optical band (second panel), the X-ray band (third and fourth panel) and the TeV band (bottom). Some of the *RXTE*/ASM and *Swift*/BAT flux points have been re-binned for better visibility. Two phases of activity can be identified in the X-ray and TeV bands (phases 1 and 2). The vertical dotted line indicates the maximum of the hard X-ray flux (*Swift*/BAT, phase 1). During phase 2 a very good X-ray/TeV coverage was achieved, where the X-ray observations were partly triggered by VERITAS.

(A color version of this figure is available in the online journal.)

calculated fluxes (for the zenith-angle range of 40 deg –60 deg) are derived (extrapolated) based on the measured spectral shapes ($dN/dE = I_0 \cdot (E/1\,\mathrm{TeV})^{-\Gamma} \cdot \exp(-E/E_{\mathrm{cut}})$). Therefore, an increased systematic error on the integral flux of ∼30% for $z > 45$ deg and ∼40% for $z > 55$ deg is assumed. Given these facts, we do not determine a quantitative value for the flux doubling times observed during this flare.

Spectral variability. To investigate a possible change of the spectral shape as a function of flux state, the data are divided into subsets according to different flux levels. The separation into flux intervals is chosen such that reasonable statistics are guaranteed for each subset. An energy spectrum is derived (see Section 2.1) for each subset and is subsequently fit by a power-law function with exponential cutoff $dN/dE = I_0 \cdot (E/1\,\mathrm{TeV})^{-\Gamma} \cdot \exp(-E/E_{\mathrm{cut}})$. A fit of a simple power-law function can be excluded with high confidence for most of the spectra (see as an example the dotted line in Figure 5, resulting in a $\chi^2/\mathrm{dof} = 264.3/15$). The results of the fits are summarized in Table 2 and the energy spectra are shown in Figure 5. No correlation between the cutoff energy E_{cut} and the flux normalization I_0 can be claimed. The spectra are also fitted with the same function by fixing the cutoff energy to $E_{\mathrm{cut}} = 4\,\mathrm{TeV}$ (Table 2). In this case, a hardening of the spectrum with increasing flux level can be seen, see Figure 6. A linear correlation between the flux and the index Γ is disfavored ($\chi^2/\mathrm{dof} = 44.6/5$, $p = 1.7 \times 10^{-08}$) as compared to a quadratic

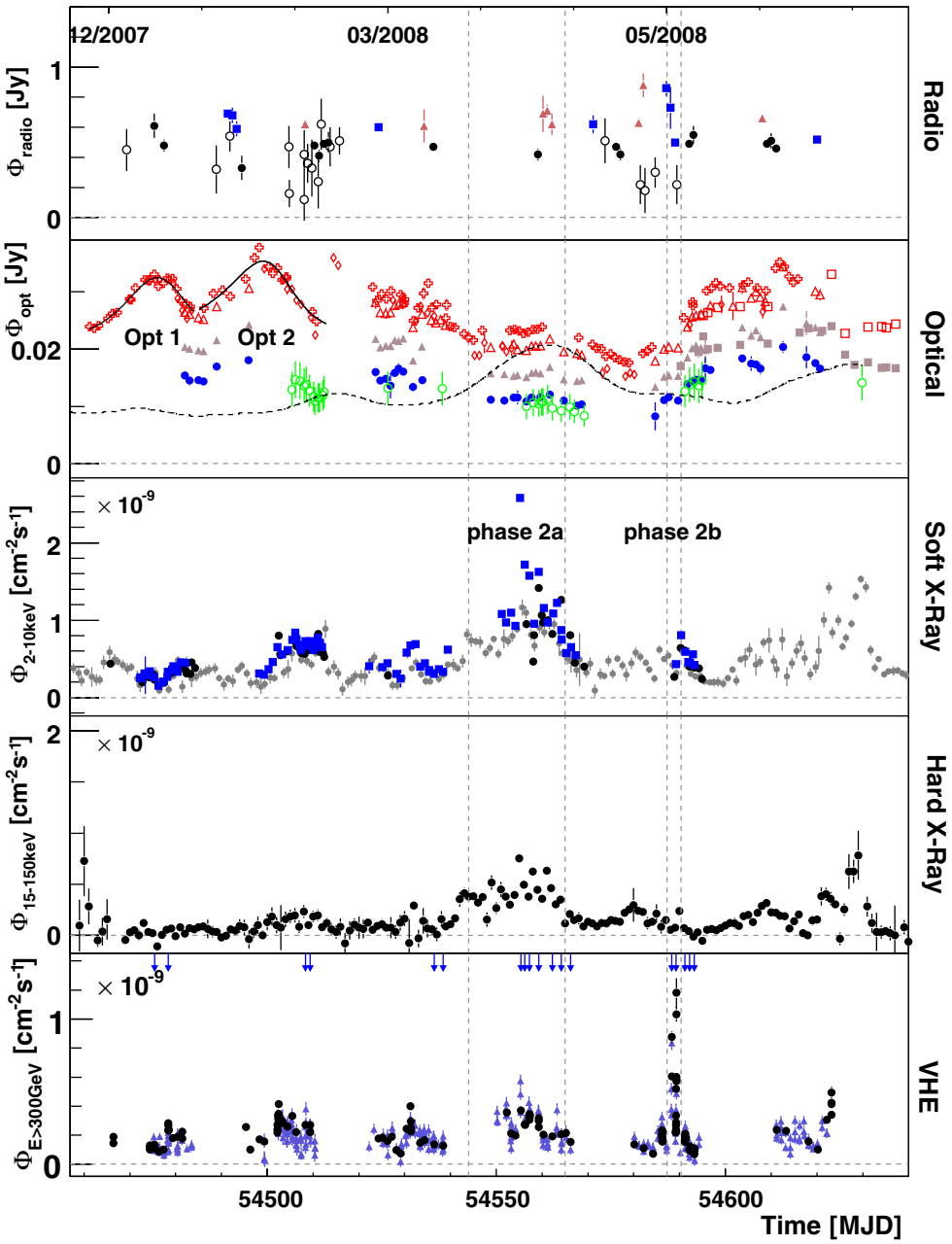

Figure 2. 2008 Mrk 421 light curves. For details see caption and legends in Figure 1. The vertical lines enclose phases of enhanced X-ray (phase 2a) and enhanced TeV (phase 2b) activity; see Figure 3 for a zoomed view of these phases. An exponential rise/fall function was fitted to the optical *R*-band Tuorla/KVA data ("Opt 1" and "Opt 2," see discussion in Section 3.4 and fit results in Table 3). The dashed line represents the optical rise/fall function folded with the ASM X-ray (dwell-by-dwell) light curve (see the text for discussion). The vertical arrows pointing downward in the bottom panel indicate the dates for which we compiled quasi-simultaneous SEDs and modeled them with a SSC code (see Figures 11 and 12).

(A color version of this figure is available in the online journal.)

relationship $\Gamma(I_0) = a + b \cdot I_0 + c \cdot I_0^2$ with $a = 2.70 \pm 0.04$, $b = (-5.3 \pm 0.6) \times 10^9$, and $c = (1.08 \pm 0.20) \times 10^{19}$ (χ^2/dof $= 13.2/4$, $p = 0.01$). This finding indicates that the spectral hardening with flux level flattens at very high flux values, as was seen already in the case of PKS 2155-304 (Aharonian et al. 2009b). Given the sparse sampling during most of the nights, we were not able to further separate the data into rising and falling (with time) flux states which may have an effect on the $\Gamma(I_0)$ function. However, the general flux versus Γ trend is in good agreement with earlier results obtained with the Whipple 10 m telescope (Krennrich et al. 2002) which are also shown in Figure 6.

Mrk 421 is detected by VERITAS (on average) with a statistical significance well above 10 standard deviations per run, even for runs with a duration of only 10 minutes. This enables a run-by-run derivation of the energy spectrum on time intervals of 10 minutes or less. Any energy spectrum derived from an individual data run which meets the following requirements is fit by a power law with exponential cutoff (the cutoff energy again being fixed to $E_{\rm cut} = 4$ TeV): (1) a differential flux point is only considered in a fit if the statistical significance of the excess is above two standard deviations; (2) an energy spectrum is only fit if at least four differential flux points fulfill the first criterion. The results of the energy spectra derived for the individual runs

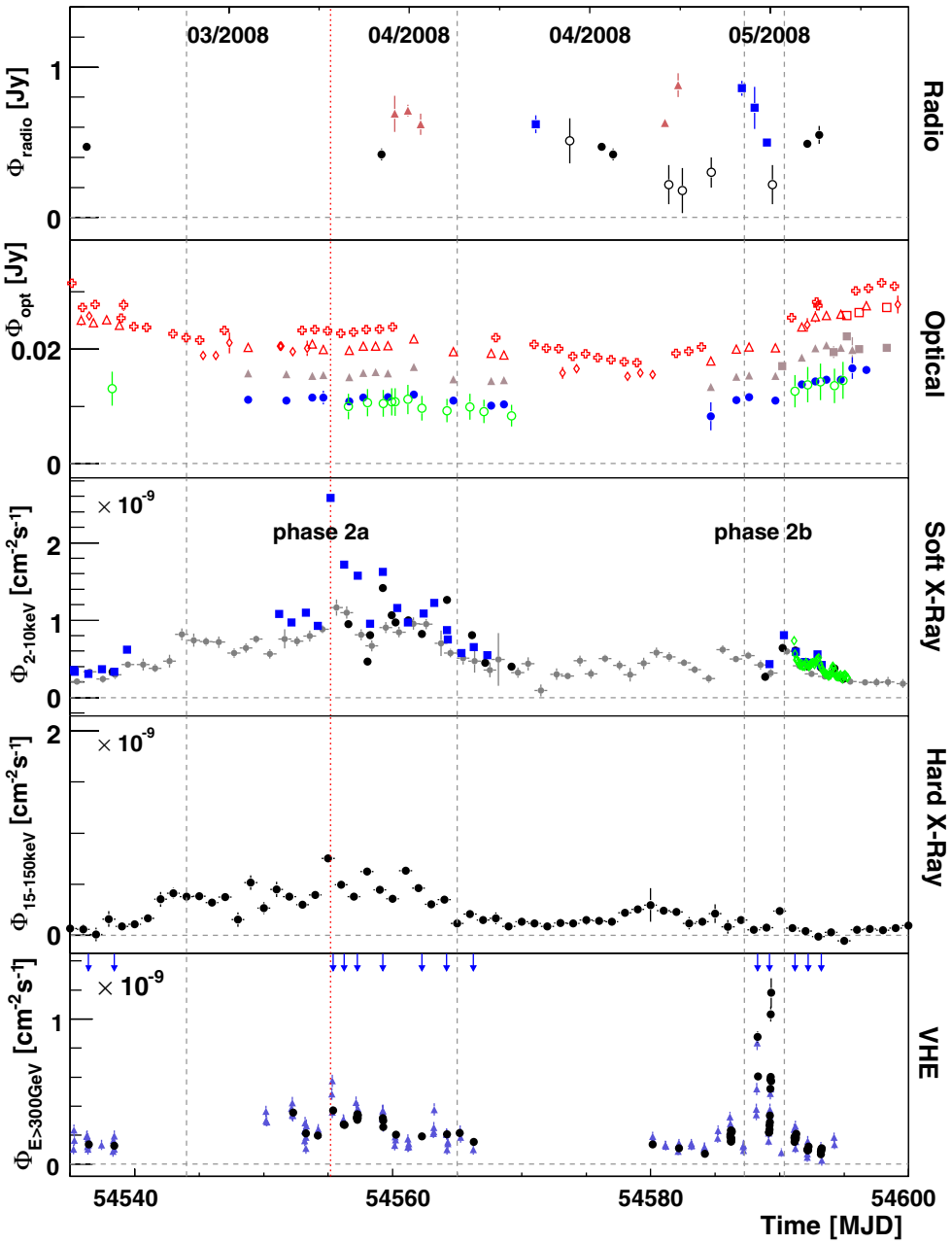

Figure 3. Mrk 421 light curves measured during the X-ray/TeV flaring state in 2008 April/May (phase 2). For details see caption and legends in Figure 1. The vertical dotted line highlights the brightest X-ray flare observed with the *RXTE*/PCA. The vertical arrows pointing downward in the bottom panel indicate the dates for which we compiled quasi-simultaneous SEDs and modeled them with a SSC code (Figures 11 and 12).

(A color version of this figure is available in the online journal.)

are shown in Figure 6 (gray points) and confirm the trend which has been found already in the data sets divided according to the different flux levels.

For both cases, the correlation coefficient was calculated and the corresponding non-directional chance probability for the null hypothesis p (non-correlation) was calculated using the Student t-distribution.[50] The correlation coefficients are $r = -0.86$ for the data sets separated by flux level,[51] and $r = -0.55$ ($p < 10^{-4}$) for the distribution based on the run-by-run data sets.

3.3. Temporal and Spectral Variability in the X-Ray Band

Energy spectra and fluxes. The *RXTE*/PCA spectra were fitted in an energy range of 3–20 keV, while the *Swift*/XRT spectra were fitted between 0.4 and 10 keV. Two models were tested to fit the data: a power law $\Phi(E) = kE^{-\Gamma}$ and a log-parabolic model $\Phi(E) = kE^{-(a+b\log(E/E_0))}$ (Massaro et al. 2004, 2006). The log-parabolic function uses an energy-dependent photon index $\Gamma(E) = a + b\log(E/E_0)$, the parameter b defines the curvature in the logarithmic parabola and a is the spectral

[50] Note: The correlation factor does not account for the statistical errors on the individual data points.

[51] Since this sample consists of only seven data pairs no chance probability p was calculated for r.

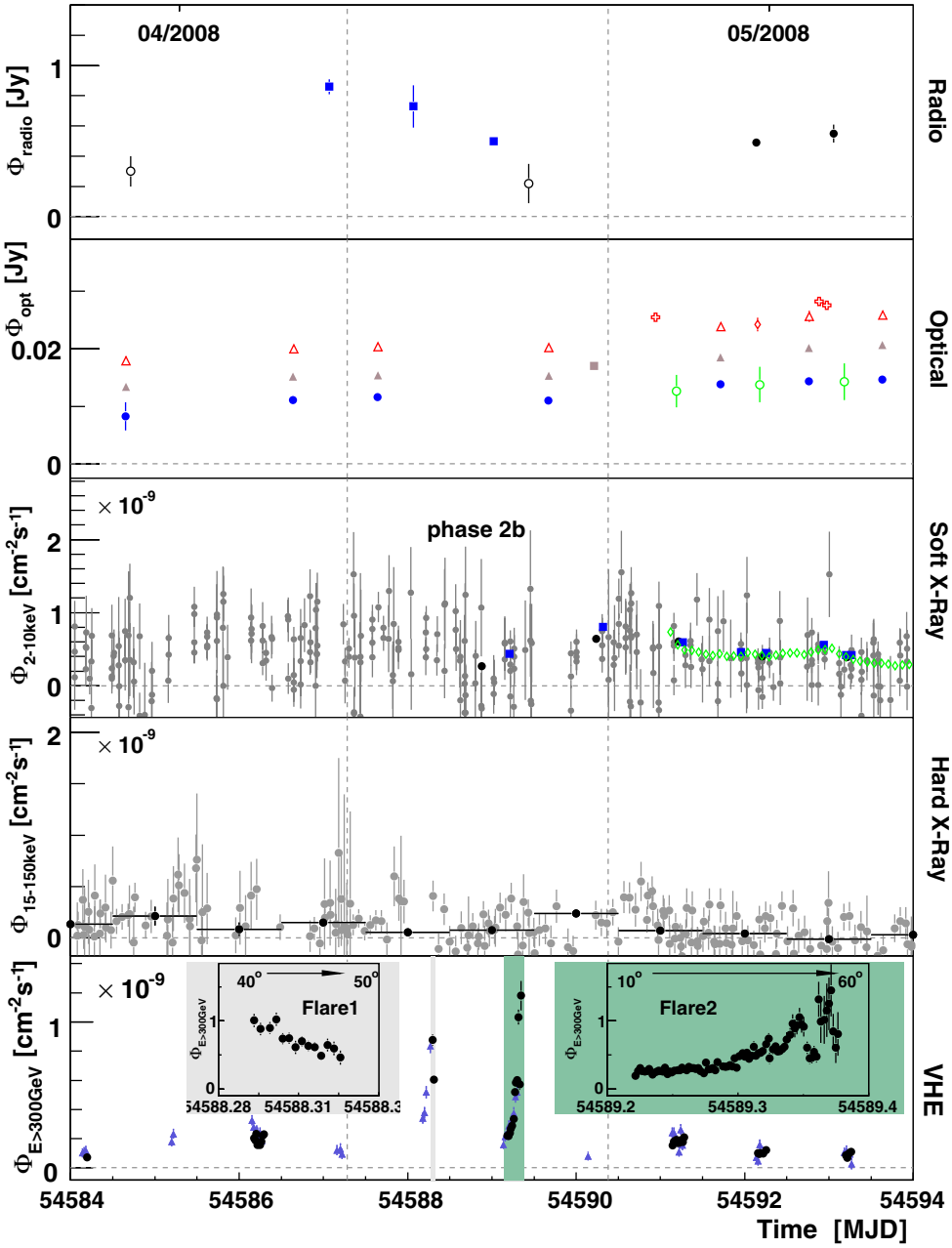

Figure 4. Mrk 421 light curves measured during the TeV flaring state in 2008 April/May (phase 2b). For details see caption and legends in Figure 1. Note, that the highest TeV flux around MJD 54590 was not accompanied by an increase in X-ray activity (compare with Figure 10). The continuous *Suzaku*/XIS soft X-ray monitoring (starting 2 days after the strong TeV flare) is shown, as well. The insets in the lowest panel show the VERITAS TeV light curves in a 3 minute binning, covering the flaring time span indicated by the colored, vertical boxes. The flares were recorded under mostly large zenith angles (indicated by the arrows) with a correspondingly higher systematic error on the flux, see the text for more details.

(A color version of this figure is available in the online journal.)

index at E_0. Both models account for absorption assuming a fixed galactic column density of 1.61×10^{20} cm^{-2} (Lockman & Savage 1995). The mean reduced χ^2 values from log-parabolic fits to *Swift*/XRT and *RXTE*/PCA data are 1.20 (96 dof) and 0.87 (161 dof), respectively. These are significantly lower than the respective mean reduced χ^2 values from power-law fits of 1.80 and 1.35. Hence, the integral flux from 2–10 keV was calculated for each observation from log-parabolic fits.

Flux variability and light curves. The X-ray light curves of the 2–10 keV fluxes are shown in Figures 1–4. Significant day timescale flaring is seen in many months in both 2006 and 2008, while for the observations in 2007 the Mrk 421 X-ray flux remained relatively low. Of particular interest are the observations in 2008 March to May. *RXTE*/PCA recorded one of the highest ever X-ray fluxes for Mrk 421 on 2008 March 30 (phase 2a). However, during the very high TeV γ-ray flux state measured by VERITAS in early 2008 May (phase 2b) the near-simultaneous X-ray flux was only found to be at a moderate level.

For all but one case the *RXTE* observation exposures were shorter than 1.5 hr (with an average exposure of 25 minutes). The *Swift* observations had a far larger range in exposures, from 15 minutes in many observations to over 40 hr in each of seven observations; the average exposure per pointing was 3.3 hr.

Table 2
Parameters and Statistical Errors of Fits $dN/dE = I_0 \cdot (E/1\,\mathrm{TeV})^{-\Gamma} \cdot \exp(-E/E_{\mathrm{cut}})$ to the Energy Spectra Shown in Figure 5: Observation Time T_{live}, Statistical Significance of the Excess in the Data Set, Flux Normalization I_0, Photon Index Γ, Cutoff Energy E_{cut}, and the Quality of the Fit

Flux State ID	T_{live} (hr)	Sign. (σ)	I_0 ($\frac{10^{-11}}{\mathrm{cm^{-2}\,s^{-1}\,TeV^{-1}}}$)	Γ	E_{cut} (TeV)	χ^2/dof
Very low state	7.83	77.62	4.78 ± 0.73	2.29 ± 0.11	1.59 ± 0.34	17.8/11 (1.62)
			3.056 ± 0.086	2.608 ± 0.033	4 ± 0	29.2/12 (2.44)
Low state	16.3	181.3	7.60 ± 0.33	2.285 ± 0.035	2.95 ± 0.29	20.7/14 (1.48)
			6.769 ± 0.084	2.375 ± 0.015	4 ± 0	29.3/15 (1.95)
Mid-state	7.79	160.6	10.26 ± 0.44	2.278 ± 0.037	4.36 ± 0.58	14.9/15 (0.99)
			10.54 ± 0.15	2.256 ± 0.017	4 ± 0	15.4/16 (0.96)
High-state A	1.38	73.0	19.08 ± 2.63	2.01 ± 0.12	1.91 ± 0.41	15.6/12 (1.30)
			13.53 ± 0.38	2.295 ± 0.037	4 ± 0	24.0/13 (1.84)
High-state B	0.63	47.3	22.23 ± 2.42	1.88 ± 0.24	3.06 ± 1.07	13.4/6 (2.24)
			20.77 ± 1.14	2.053 ± 0.080	4 ± 0	143.0/7 (2.00)
High-state C	0.63	53.76	21.74 ± 1.97	2.40 ± 0.26	9.6 ± 9.0	0.9/6 (0.15)
			23.96 ± 1.62	2.05 ± 0.09	4 ± 0	2.7/7 (0.39)
Very high state	0.63	63.5	35.77 ± 3.08	1.87 ± 0.17	2.74 ± 0.60	6.2/9 (0.69)
			32.0 ± 1.2	2.111 ± 0.057	4 ± 0	8.7/10 (0.87)

Notes. The second row for each flux state corresponds to a fit in which the cutoff energy was fixed to a value of $E_{\mathrm{cut}} = 4$ TeV.

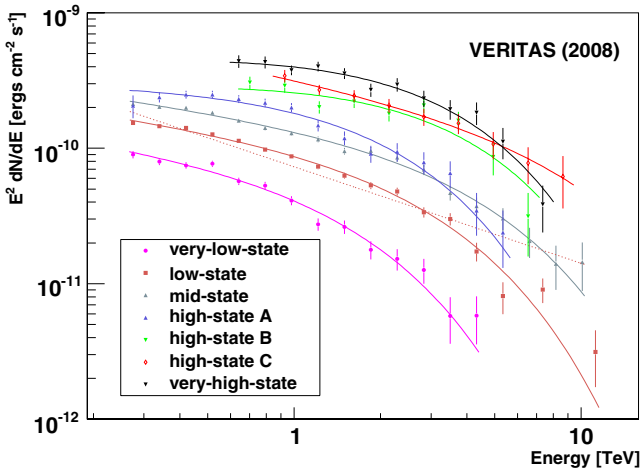

Figure 5. Time-averaged VERITAS energy spectra for different flux levels. Only data taken in 2008 are used. A power law with exponential cutoff is fit to each spectrum (curves), the fit parameters and statistical errors are summarized in Table 2. The dotted line shows a power-law fit to the low-state spectrum to illustrate the incompatibility of this model and the data. The high-flux spectra were taken at zenith angles $z > 35$ deg with a correspondingly higher energy threshold.

(A color version of this figure is available in the online journal.)

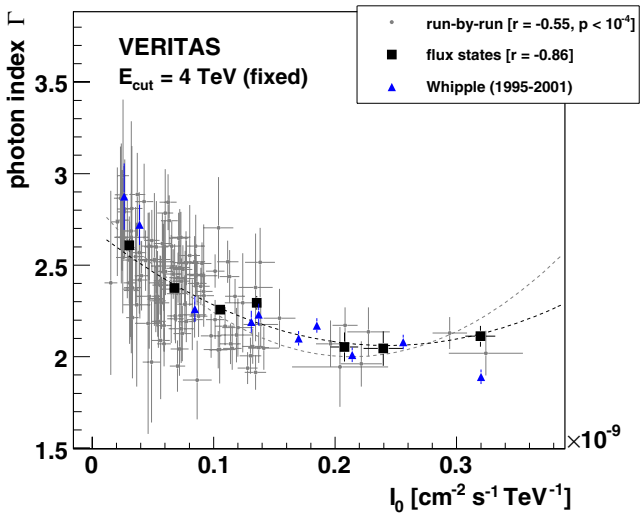

Figure 6. Photon index Γ vs. flux normalization I_0 (at 1 TeV) obtained from a power-law fit with exponential cutoff (fixed to $E_{\mathrm{cut}} = 4$ TeV, statistical errors only). Each gray data point corresponds to a data run with a duration of 10–20 minutes. The black points correspond to the values obtained from the fits to the spectra grouped according to their flux states (defined in Figure 5 and Table 2). Correlation coefficients r and the corresponding chance probabilities for the null hypothesis (no correlation) are given in the legend. Results obtained from earlier Whipple 10 m observations (Krennrich et al. 2002) are shown for reference.

(A color version of this figure is available in the online journal.)

Significant variability in both *RXTE*/PCA and *Swift*/XRT observations was found. The corresponding *Swift* observations spanned up to 3 days, with clear flaring in the rates on hour timescales. Some of the *RXTE*/PCA light curves show a steady change in the count rate over 20 minute periods. However, more detailed studies of the sub-day flux variations in the X-ray data are beyond the scope of this paper.

Spectral variability. Drawing from this large set of X-ray observations, the correlation of X-ray flux to spectral shape is investigated here. This will allow identification of trends which could give important input to the modeling. The left panel of Figure 7 shows the correlation plot between the log-parabola parameters a (index) versus the 2–10 keV flux. The corresponding correlation plot between the curvature parameter b and the flux is shown in the right panel of Figure 7. Although the index a is not independent of the curvature parameter b, the conclusion can be reached that an increased flux is accompanied by a hardening of the spectrum (parameter a) since there is only a moderate correlation between the flux and b. This finding is compatible with earlier findings (Fidelis & Iakubovskyi 2008). The (anti)correlation between a and the flux is significant: the non-directional chance probability of the derived correlation coefficient for the null-hypothesis is $p < 10^{-4}$ for the *RXTE*/PCA data as well as for the *Swift*/XRT data.

3.4. Flux Correlation Analysis

This section describes the search for flux correlations between the light curves measured in different energy bands and is based on the light curves shown in Figures 1–4.

Radio/optical/TeV flux correlations. As can be seen in Figure 1 there is no significant variation in the radio flux on day, week, or month timescales. Thus, no significant correlation with

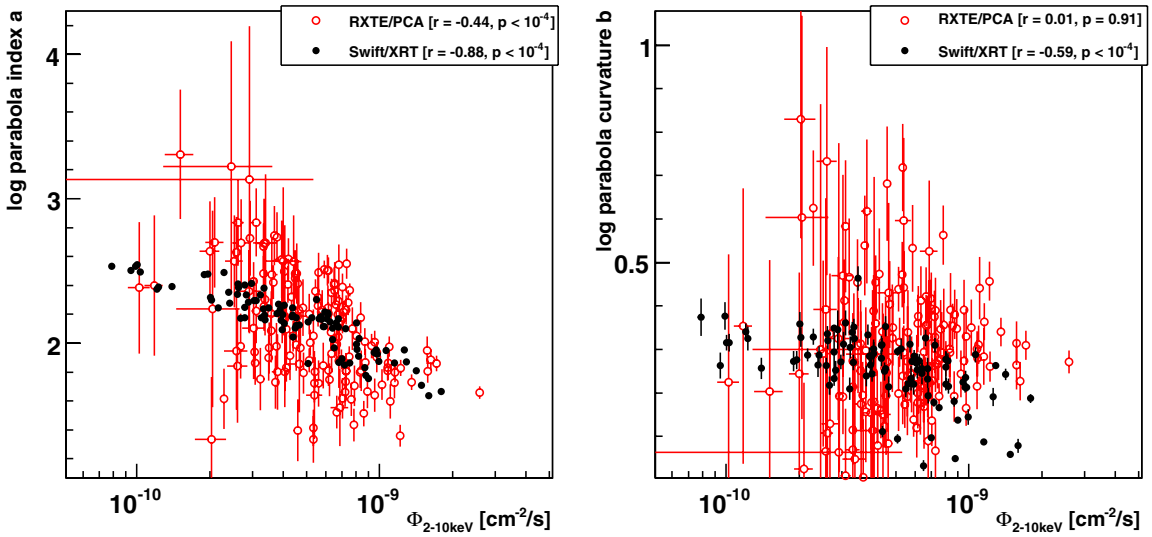

Figure 7. Correlations between the spectral shape and the flux level for the X-ray data sets taken with *RXTE*/PCA and *Swift*/XRT. Correlation coefficients r and the corresponding chance probability for the null hypothesis (no correlation) are given in the legends. Left: the log-parabola parameter a vs. the 2–10 keV photon flux. Right: the log-parabola curvature parameter b vs. the 2–10 keV photon flux.

(A color version of this figure is available in the online journal.)

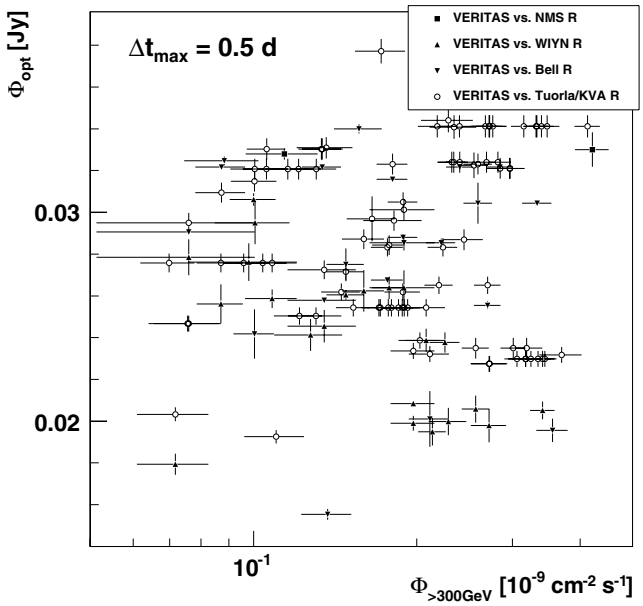

Figure 8. Correlation between TeV and optical fluxes. The maximum allowed time difference between the data points is $\Delta t \leqslant 0.5$ days.

fluxes measured in the other wave bands is found. This could be explained if (1) the dominant portion of the radio emission does not originate from the inner jet region that likely produces the flux variability in the other energy bands, or (2) structures in the light curve are smeared out due to slower cooling of the radio emitting electrons compared to the electrons responsible for the shorter wavelength emission (see Section 4).

The optical fluxes, on the other hand, show clear variability on timescales of weeks (Figure 2), where the fluxes from the different bands (R, B, and V) are clearly correlated. This is not surprising since the frequency filter bands are not largely separated in terms of photon energy and a common origin of the radiation in the three bands can be assumed. Figure 8 shows the correlation plot between the VERITAS TeV γ-ray fluxes and the optical fluxes in the R band. A maximum time gap between the TeV and optical measurements of $\Delta t \leqslant 0.5$ days was allowed for the individual data pairs. The corresponding correlation factors are compatible with chance expectations. A similar correlation study between X-ray and optical fluxes did not result in any significant correlation coefficient, either. Given the different timescales of the flux variations (sub-day level in the X-ray and TeV band, and weeks in the optical band), the lack of a direct flux correlation is expected.

Except for the *Swift*/UVOT data the contribution of the host galaxy is not subtracted. Since it has to be constant in time, the light curves can be used to set an upper limit on the baseline, which in turn would be an upper limit on the host galaxy contribution in the measured data. This contribution is estimated to be 0.009 Jy (R band, see dotted line in Figure 1), 0.009 Jy (V band), and 0.006 Jy (B band). These estimates are somewhat lower as compared to the modeling of Nilsson et al. (1999) who estimate 0.014 Jy for the R band.

Although neither instantaneous nor delayed correlation between the optical and the X-ray/TeV bands was found, it is important to study the structure of the optical light curves. Two well-defined flares[52] "Opt 1" and "Opt 2" (Figure 2) were fitted with an exponential rise/fall function $\Phi_{\rm opt}(t) = a + b/(\exp(-\frac{t-T_0}{\tau_{\rm r}}) + \exp(\frac{t-T_0}{\tau_{\rm f}}))$. The fit parameters are summarized in Table 3, showing that the optical flux changes on timescales of less than 10 days with the indication of slightly shorter fall times $\tau_{\rm f}$ as compared to the rise times $\tau_{\rm r}$.

These timescales are on the same order as the estimated value of ∼15 days (assuming the same electron population), based on the characteristic X-ray/TeV variability timescale of $\leqslant$0.5 days (see the discussion in Section 4). One can interpret $\Phi_{\rm opt}(t)$ as a "characteristic" optical response to a single X-ray/TeV flare. With this assumption a hypothetical prediction can be made for the optical light curve by folding $\Phi_{\rm opt}(t)$ (using $\tau_{\rm r} = 7$ days and $\tau_{\rm f} = 5$ days, and a delay $\Delta T = 7$ days) with the X-ray and/or TeV γ-ray light curves. The prediction based on the frequently sampled *RXTE*/ASM X-ray light curve (dwell by dwell, MJD 54450–54630, linear interpolation between the flux points) is shown together with the optical light curve in

[52] A third flare occurring around MJD 54149 was also fitted, resulting in comparable structural properties as listed in Table 3.

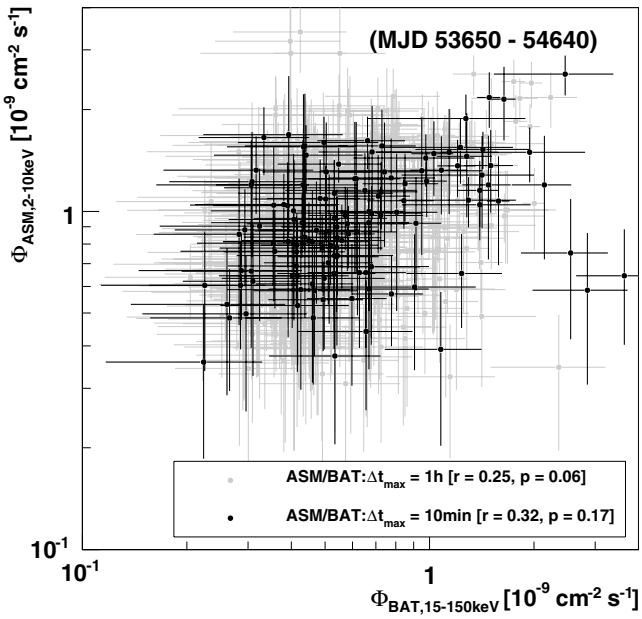

Figure 9. Hard/soft X-ray flux correlation between the 15–150 keV *Swift*/BAT flux and the 2–10 keV *RXTE*/ASM flux. All dwell-by-dwell flux points with a statistical significance above 2σ measured in the first half of 2008 (MJD 54457–54640) are shown for two cases of a maximum time lag between the observed data points. The legend gives the corresponding correlation coefficient and the corresponding chance probability for the non-correlation.

Table 3
Parameters of an Exponential Rise/Fall Function (Section 3.4)
$\Phi_{\rm opt}(t) = a + b/(e^{-(t-T_0)/\tau_{\rm r}} + e^{(t-T_0)/\tau_{\rm f}})$ Fitted to the Optical Flares "Opt 1" and "Opt 2" (Figure 2)

Parameter	Opt 1	Opt 2
a (Jy)	0.021 ± 0.001	0.023 ± 0.001
b (Jy)	0.023 ± 0.002	0.024 ± 0.003
$\tau_{\rm r}$ (day)	7.16 ± 1.78	9.52 ± 1.35
$\tau_{\rm f}$ (day)	5.46 ± 0.80	4.46 ± 0.77
T_0 [MJD]	54476.8 ± 1.4	54501.4 ± 0.7

Figure 2 (arbitrary units)—no agreement is found. A caveat should be mentioned: the *RXTE*/ASM flux measurements are not very accurate; however, the general trends (high versus low state) should allow the comparison of the two different wave bands. $\Phi_{\rm opt}(t)$ was also folded with the TeV γ-ray light curve (MJD 54500–54630, linear interpolation between the flux points). Again, no correlation can be found. There is a caveat here, as well: the non-continuous sampling of the TeV γ-ray light curve and the short duty cycle of flares results in a considerable chance that one or more strong γ-ray flares have been missed which would change the shape of the folded optical light curve. Therefore, the latter results are not shown in Figure 2. Furthermore, our above comparison ignores the possibility that particles with different energies are injected at the beginning of the flare.

Hard/soft X-ray flux correlations. The correlation between hard and soft X-ray fluxes is studied based on the dwell-by-dwell flux points measured with *Swift*/BAT (15–150 keV) and *RXTE*/ASM (2–10 keV). The correlation plot including all data points taken in spring 2008 (MJD 54457–54640, contemporaneous with the VERITAS coverage) with a statistical significance of more than two standard deviations is shown in Figure 9. The distribution was generated for two different requirements regarding the maximum allowed time gap between

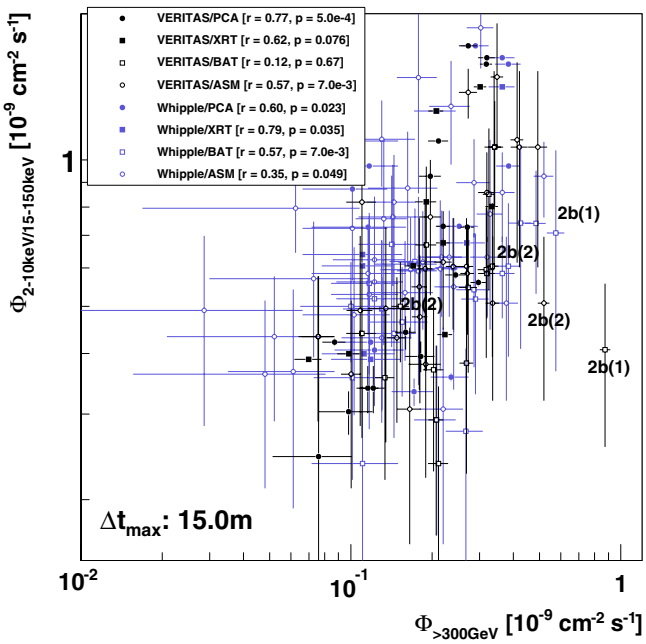

Figure 10. Correlation between TeV fluxes (VERITAS and Whipple) and X-ray fluxes (*RXTE*: PCA and ASM, *Swift*: XRT and BAT). All X-ray fluxes are given between 2 and 10 keV, except for the *Swift*/BAT fluxes which are given between 15 and 150 keV. Only data measured in the first half of 2008 (MJD 54457–54640) are shown. The *RXTE*/ASM and *Swift*/BAT fluxes are dwell by dwell with the requirement that the statistical significance is above two standard deviations. The maximum time difference between the data points is $\Delta t \leqslant 15$ minutes. The correlation coefficients including the chance probability for the null hypothesis are shown in the legend. The flux pairs measured during the first (2b(1)) and second night (2b(2)) of phase 2b are marked.

(A color version of this figure is available in the online journal.)

the center time of the individual pointings ($\Delta t \leqslant 1$ hr and $\Delta t \leqslant 10$ minutes). In both cases, indications for only a weak correlation of $r \simeq 0.1$ are found with moderate significance. However, while the *RXTE*/ASM data are testing the falling edge of the synchrotron peak in the SED, the *Swift*/BAT data likely fall into the transition zone between synchrotron and high-energy peaks, compare with Figures 11 and 12.

X-ray/TeV flux correlations. The rich data sets allow for a detailed study of the X-ray versus TeV flux correlations. The TeV runs have a duration of 10–20 minutes. With a few exceptions (during the highest flare) no indications for TeV flux variations were found within any of the runs. A maximum time lag between the correlated X-ray/TeV data points of $\Delta t \leqslant$ 15 minutes was allowed (close to the average TeV run duration). Since some of the dedicated, high-quality data from *Swift*/XRT and *RXTE*/PCA were considerably longer in exposure, an additional cut on the total length of the X-ray pointing was applied (based on the average exposure per pointing): $\Delta T \leqslant 30$ minutes in the case of *RXTE*/PCA and $\Delta T \leqslant 2$ hr in the case of *Swift*/XRT. Flux variations within individual X-ray pointings are not investigated in the framework of this paper; therefore, the data pairs cannot be considered as exactly simultaneous. The *RXTE*/ASM and *Swift*/BAT dwell-by-dwell data points have exposures of the order of 1–10 minutes, so that no cut on ΔT was applied in those cases. Individual *RXTE*/ASM and *Swift*/BAT flux measurements were only considered in the case of a significance level of $\geqslant 2\,\sigma$. The results discussed below do not strongly depend on the exact choice of Δt and ΔT.

Figure 10 shows the flux correlations for the data taken in spring 2008 (MJD 54457–54640). The correlation coefficients

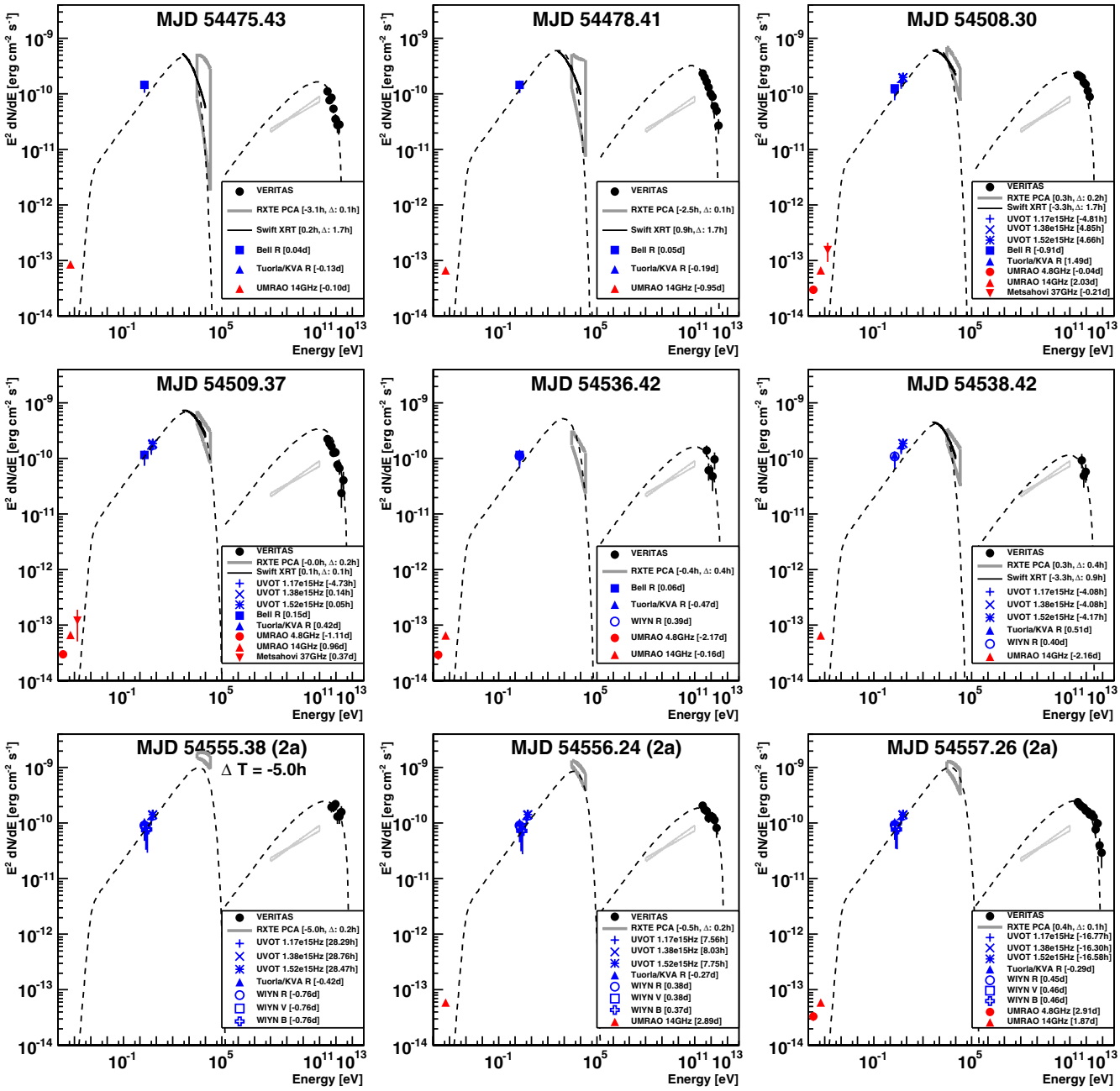

Figure 11. SEDs of Mrk 421 for individual dates showing all available MWL data (statistical errors only) if the corresponding time lag criterion is met (see the text for more detail). The legends indicate the time lags $\Delta T = T_{\rm MWL} - T_{\rm TeV}$ between the individual MWL data and the VERITAS data. For the X-ray observations, the duration of the pointing Δ is given, as well. The number in parentheses following the MJD (if given) refers to the phase (2a or 2b, see Figure 3) in which the data were taken. The SEDs were fit by a one-zone SSC model (dashed curves); the corresponding model parameters are summarized in Table 4. The non-simultaneous MeV/GeV spectrum measured by *Fermi* (2008 August to 2009 July) is shown for reference (Abdo et al. 2010).

(A color version of this figure is available in the online journal.)

and the corresponding non-directional chance probability for the null hypothesis (no correlation) were calculated and are shown in the figure legend. The X-ray and TeV fluxes seem to be correlated ($r > 0.5$ for most data subsets) with chance probabilities of the order of a few percent or below. The VERITAS/BAT data set is the only one which is not correlated in a significant manner. One of the high TeV flux points measured during the strong TeV γ-ray flare (Figure 4) was accompanied by a *Swift*/BAT dwell-by-dwell pointing ($\Delta t \leqslant 3.4$ minutes), which however did not indicate an increased activity in the hard X-ray band. The *Swift*/BAT point has a duration of 8 minutes and is therefore fully contained in the time interval of the corresponding VERITAS data run of 20 minute duration. This flux pair is located in the lower right corner of Figure 10 (labeled as 2b(1)) and may be seen as the indication of an orphan TeV γ-ray flare. However, since this indication is based on only one X-ray/TeV flux pair measured during a high TeV γ-ray flux state, there is not enough evidence for a strong claim. If the corresponding data pair were removed, the VERITAS/BAT flux correlation would increase to $r = 0.62$ with a chance probability of $p = 0.019$. Other flux pairs from the two TeV flare nights (phase 2b) are indicated in Figure 10, as well.

Discrete correlation functions (DCF). The light curves were also analyzed using the DCF technique (Edelson & Krolik 1988)

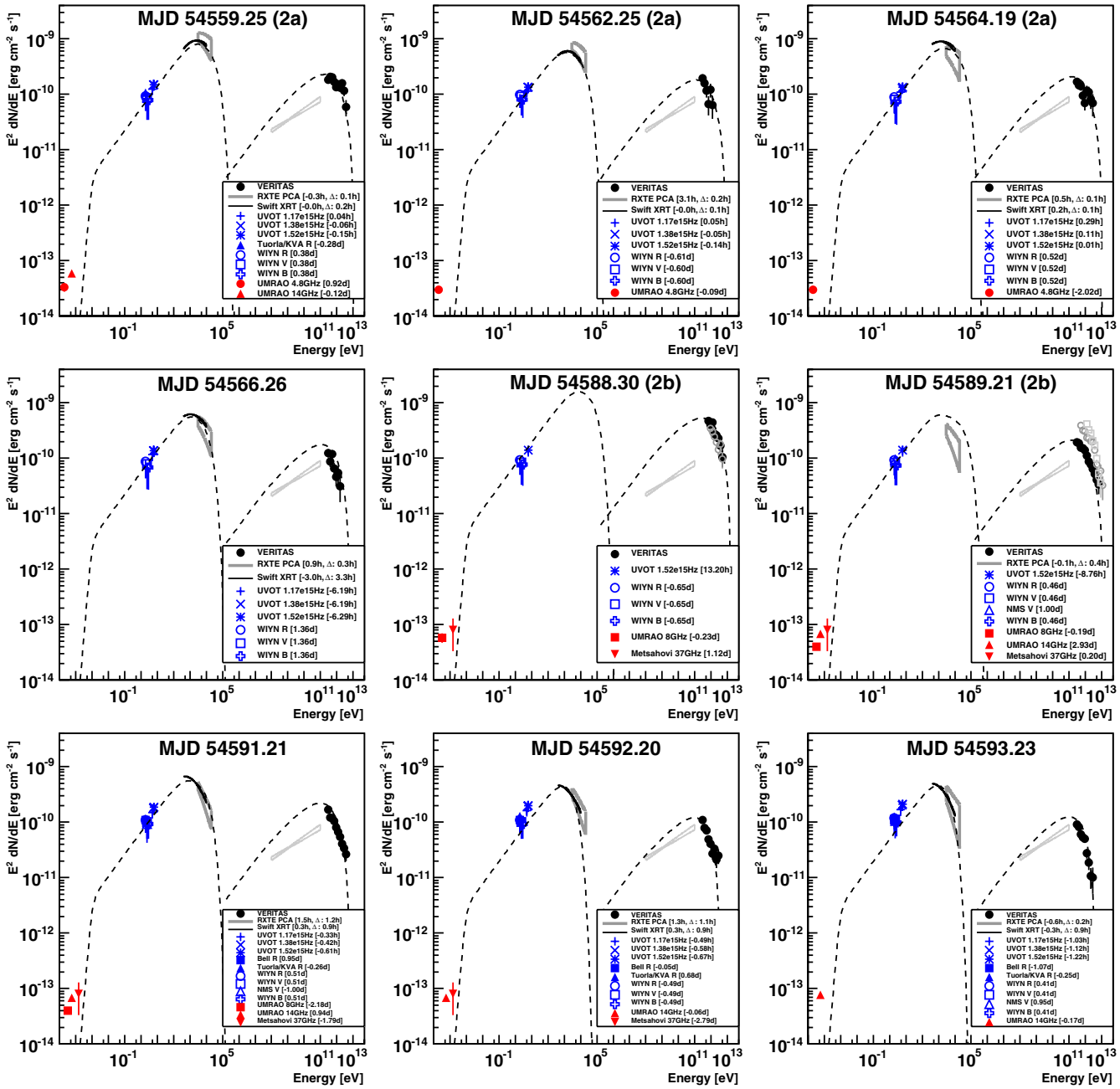

Figure 12. SEDs of Mrk 421, continued from Figure 11. The SEDs of the two flare nights are also shown: MJD 54588.30 (no X-ray coverage in this night) and MJD 54589.21 with X-ray coverage during the onset of the flare (solid TeV points) but not during the high flare state (open TeV data points).
(A color version of this figure is available in the online journal.)

in order to search for correlated/delayed emission between different energy bands, allowing for significant time lags (i.e., one light curve having the delayed shape of another one). The radio, optical, and X-ray light curves were tested against the TeV γ-ray light curve. Except for the zero lag X-ray/TeV correlation (see above) no significant time lag and/or correlation at zero time lag was found for the radio and optical bands as compared to the TeV γ-ray emission.

3.5. Spectral Energy Distributions and Modeling

The SEDs showing the VERITAS and MWL data were generated for individual nights and plotted in Figures 11 and 12. Based on the different variability timescales, data from the different wave bands are plotted in the quasi-simultaneous SEDs if the time lag Δt between the MWL data and the TeV data is $\Delta t_{\text{X-ray}} \leqslant 0.15$ days (X-ray), $\Delta t_{\text{opt}} \leqslant 1.5$ days (optical), and $\Delta t_{\text{radio}} \leqslant 3$ days (radio). Shorter time lags are present (down to real simultaneity) and the exact times are given in the figure legends of the SEDs. The time spans (duration) of the X-ray observations are given in the legends, as well. Possible spectral variations within individual X-ray observations are beyond the scope of this paper and are ignored in the modeling of the SEDs. The X-ray spectra (*Swift*/XRT and *RXTE*/PCA) were fit with a log-parabola model $\Phi(E) = kE^{-(a+b\log(E))}$, and the corresponding log-parabola bowties including the statistical errors of the fits are shown if the fit resulted in a $\chi^2/\text{dof} < 2$. All errors are statistical only.

As a reference, Figures 11 and 12 also show the non-simultaneous MeV/GeV energy spectrum measured by the *Fermi*/LAT (Atwood et al. 2009) in 2008 August to 2009 July (Abdo et al. 2010). During this period, the LAT detects Mrk 421 with a statistical significance of 88σ and the energy spectrum is well fit by a power law in the whole energy range (curvature index given in the *Fermi* catalog of 0.72). Interestingly, the variability index of 43.9 does not indicate very strong variability during the above period, so that the *Fermi*/LAT energy spectrum shown in the SEDs may give a realistic indication for a low/medium flux state of Mrk 421. However, given the non-simultaneity of the *Fermi* observations, the MeV/GeV spectrum was not included in the modeling.

The SEDs were fit with a one-zone SSC model following Krawczynski et al. (2004). In this model a spherical emission region of radius R is filled with a relativistic electron population, traveling down the jet with a bulk Lorentz factor Γ ($\beta = v/c$). The magnetic field B in the emission region is randomly oriented. The emitted radiation is Doppler-shifted by $\delta = [\Gamma(1 - \beta\cos\theta)]^{-1}$, θ being the angle between the jet axis and the line of sight of the observer. The electron distribution is normalized by a factor u_e (in units of erg cm^{-3}) and is described in the jet frame by a broken power law with $E_{\rm min}$, $E_{\rm brk}$, and $E_{\rm max}$ and the two corresponding spectral indexes $\alpha_1 = -2.2$ and $\alpha_2 = -3.2$. Mrk 421 is located at a redshift of 0.031 so that the energy-dependent pair absorption on photons of the extragalactic background light (EBL) cannot be neglected. EBL absorption is taken into account in the model following Franceschini et al. (2008). Since most of the optical data were not corrected for the contribution of the host galaxy, the optical data points have to be seen as an upper limit on the jet emission region. The estimate on the host galaxy contribution (Section 3.4) has been added as a systematic error. The SSC model was adjusted to the SEDs with the following procedure.

1. In a first step, the three SEDs with the smallest time lags between the X-ray and the TeV spectra (MJD 54559.25, 54562.25, and 54509.37) were used to derive a full set of model parameters. The Doppler factor was set to $\delta = 40$ and the magnetic field was set to $B = 0.2$ G, in agreement (order of magnitude) with a synchrotron cooling time of $\tau_{\rm sync}(B) \times \delta \approx T_{\rm flare} = 1$ hr for the electrons emitting the synchrotron emission close to the maximum of the SED. Then, the radius R, the energy density in electrons u_e (erg cm^{-3}), as well as $E_{\rm brk}$ and $E_{\rm max}$ were varied until the model would describe the SED (optical to TeV).
2. In a second step, the remaining SEDs were fit by only allowing variations of u_e and $E_{\rm max}$ (and in the case of bad fits also $E_{\rm brk}$) as compared to the model parameters derived above, reflecting a change in the injected electron population.

The SSC model fits are shown in Figures 11 and 12, and the model parameters for the individual SEDs are summarized in Table 4. The models generally underpredict the radio emission which is synchrotron self-absorbed in the model at the low-energy tail of the SED. This discrepancy could be explained by additional radio emission from regions in the jet not emitting the TeV radiation. Also, the synchrotron self-absorbed radio blobs could expand and lead to a delayed radio emission from a larger region (Acciari et al. 2009a), which however is not taken into account in the model.

The break energy $E_{\rm brk}$ of the electron spectrum is very near the maximum energy of the electron spectrum $E_{\rm max}$. The missing plateau ($E_{\rm brk} \sim E_{\rm max}$) is directly seen in the *Swift*/XRT data which show a direct turnover of the synchrotron peak. This is in agreement with earlier findings in the case of Mrk 421 (Fossati et al. 2008) and is in contrast to the SEDs measured in the case of Mrk 501 for which the synchrotron emission peaks at higher energies and shows indications of a plateau (Krawczynski et al. 2000). If $E_{\rm min} \ll E_{\rm brk}$, the missing plateau implies that cooling did not have time to kick in. However, if $E_{\rm min} = E_{\rm brk}$ and cooling is very efficient, electrons cool below $E_{\rm brk}$ and one gets a new "effective" $E_{\rm min} \ll E_{\rm brk}$, and the "true" $E_{\rm min}$ becomes $E_{\rm brk}$.

Table 4
Parameters of the SSC Models as Shown in Figures 11 and 12

Date MJD	u_e (erg cm^{-3})	$\log(E_{\rm max})$	$\log(E_{\rm brk})$	u_e/u_B
54475.4	0.45	10.8	10.5	283
54478.4	0.65	10.9	10.4	408
54508.3	0.50	11.0	10.6	314
54509.3	0.60	11.1	10.5	377
54536.4	0.40	11.0	10.6	251
54538.4	0.35	10.9	10.6	220
54555.4	0.40	11.2	11.2	251
54556.3	0.35	11.2	11.1	220
54557.3	0.40	11.3	11.0	251
54559.2	0.40	11.4	10.8	251
54562.2	0.40	11.3	10.6	251
54564.2	0.40	11.4	10.7	251
54566.2	0.40	11.2	10.6	251
54588.3	0.55	11.6	11.0	345
54589.3	0.43	11.5	10.6	270
54591.3	0.48	11.2	10.5	301
54592.3	0.35	11.0	10.6	220
54593.3	0.35	11.0	10.6	220

Notes. The following parameters are the same for all models: Doppler factor $\delta = 40$, magnetic field $B = 2.0 \times 10^{-5}$ $T = 0.2$ G, radius $R = 2.5 \times 10^{15}$ cm, $\log(E_{\rm min}) = 3.0$. The table shows the remaining parameters u_e, $\log(E_{\rm max})$, and $\log(E_{\rm brk})$ for the different SEDs as well as the particle energy density to magnetic field energy density ratio. $u_e/u_B = 8\pi u_e/B^2$.

All SEDs are reasonably described by using the same model parameters except for the electron normalization u_e and the break/maximum electron energies $E_{\rm brk}$ and $E_{\rm max}$ which were adjusted for each individual SED (Table 4). The only exceptions are the X-ray flare (Figure 11) and the two TeV γ-ray flare SEDs (Figure 12).

1. *MJD 54555.38:* The *RXTE*/PCA bowtie shown in this SED (Figure 11) does not qualify for the previously defined X-ray/TeV time lag criterion. However, the X-ray flux is the highest one measured during the whole MWL campaign (see dotted line in Figure 3) so that it is shown for reference (but not included in the fit). The closest Whipple TeV flux point is ~2 hr away and also does not show signs for an increased TeV flux. This may indicate an orphan X-ray flare, but the lack of simultaneous TeV data does not allow a strong conclusion.
2. *MJD 54588.3:* The SSC model slightly overpredicts the optical emission. However, the optical data are not simultaneous and the TeV fluxes can change within 20 minutes: the black data points in Figure 12 represent the first 20 minutes of the flare, whereas the open gray points represent the second 20 minutes of the flare in that night (compare with the lower left inset in Figure 4). Unfortunately, no X-ray data (*Swift*/XRT or *RXTE*/PCA) were taken during this night.

3. *MJD 54589.21:* The black data points in Figure 12 represent the low plateau at the beginning of the flare—compare with the lower right inset in Figure 4—and are the ones which were used for the fit of the SED. The *RXTE*/PCA measurement partially overlapped this time, but is overpredicted by the model. Given the generally good fits of the model, this is interesting since the VERITAS/BAT flux pairs of the same night (see 2b(2) in Figure 10) as well as the previous night (2b(1)) also indicate a possible orphan TeV γ-ray flare. The higher flux states during this flare night (open gray points in Figure 12) were not accompanied by simultaneous X-ray measurements and were therefore not modeled.

The fact that the X-ray (and optical) data are not perfectly described during the flare nights (as well as for a few other nights) may be explained by the fact that only u_e, E_{brk}, and E_{max} were allowed to vary, after the other parameters had been fixed based on the three most complete and contemporaneous SEDs, which all correspond to TeV low/medium states of Mrk 421.

4. SUMMARY AND DISCUSSION

Together with many MWL partners VERITAS conducted an intensive MWL campaign on Mrk 421 in 2008. During low states of Mrk 421, VERITAS is able to measure the source flux to an accuracy of 5% in 20 minute time intervals. In the 47 hr data set presented in this paper, we did not find evidence for rapid flux variability on timescales of minutes as reported for Mrk 501 (Albert et al. 2007) and PKS 2155-304 (Aharonian et al. 2009b). However, the only strong outburst (reaching a flux level of 10 Crab) which would have allowed testing these short timescales of flux variations was measured at high zenith angles with a strongly reduced detection sensitivity.

Two phases of enhanced X-ray (phase 1) and X-ray/TeV (phase 2) activity are found. Phase 2 can be separated into a period of strong X-ray activity without a strong TeV γ-ray flaring, followed by a TeV γ-ray flare lasting for 2 days without any indication for contemporaneous strong X-ray activity. This may indicate an X-ray (phase 2a) and TeV γ-ray (phase 2b) orphan flare, but the data are too sparse for a definite claim. In the remaining data there is significant evidence for a correlation between the X-ray and TeV fluxes.

No significant flux correlations between the TeV band and the optical/radio bands were found. Assuming that (1) the optical and X-ray/TeV photons are emitted co-spatially, and that (2) the flux variability timescale equals the radiative cooling time, one can estimate the expected relation between the observed timescales of flux variations: the mean energy of emitted photons E_{obs} scales with the electrons' Lorentz factor squared, $E_{obs} \propto \gamma^2$. The cooling time τ_{cool} scales proportional to $1/\gamma$. The energy of the X-ray photons is three orders of magnitude higher than the energy of the optical photons. The Lorentz factors of the X-ray emitting electrons should thus be 1.5 order of magnitudes (factor $\sim$30) larger than the Lorentz factors of the optically emitting electrons. If the X-rays (and γ-rays, from IC scatterings of the electrons which emit X-rays as synchrotron emission) show flux variability on a timescale of $\leqslant$0.5 days (Fidelis & Iakubovskyi 2008; Gaidos et al. 1996), then the optical fluxes should vary on a timescale of $\leqslant$15 days which is well compatible with the observed timescales in the optical and X-ray/TeV bands (Section 3.4). However, as discussed in Section 3.4, the optical light curve does not seem to be a delayed and stretched version of the X-ray light curve or the TeV γ-ray light curve, implying that the dominant fraction of the observed optical emission does not originate from the X-ray/TeV emission region. Interestingly, Rieger (2004) discusses variable (even periodic) flux variations on (periodic) timescales of $P \leqslant 10$ days which can be explained by geometrical arguments of internal jet rotation. Our data, however, seem to indicate more complicated structures than periodicity. A similar estimate using the radiative cooling time for the energies in the radio band leads to timescales of 10 years or more, impossible to test with the given MWL data set.

Clear indications for spectral hardening with increasing flux levels are found in the X-ray and TeV bands. In the TeV band, the spectral hardening seems to level out for the very high fluxes above $\sim$5 Crab. A similar trend had already been found in earlier Whipple data of Mrk 421 as well as in the strong flare of PKS 2155-304 measured by H.E.S.S. (Aharonian et al. 2009b).

The rich MWL data set presented in this paper allowed for the compilation of 18 quasi-simultaneous SEDs, well constrained by accurate *Swift*/XRT X-ray and VERITAS TeV spectra. The SEDs can be described by a one-zone SSC model with nearly one set of parameters; only u_e, E_{brk}, and E_{max} needed to be adjusted to describe the whole set of SEDs. However, for most of the SEDs Mrk 421 was found to be in low or moderate flux states, leading to similar SEDs on different days. Our SSC modeling indicates that the emission process and the jet parameters are reasonably well constrained.

So far, there are only four TeV blazars with a reasonable amount of simultaneous MWL data in order to claim a correlation between X-ray and TeV γ-ray fluxes: Mrk 421 (Fossati et al. 2008; Błażejowski et al. 2005; Horan et al. 2009), Mrk 501 (Krawczynski et al. 2002), PKS 2155-304 (Aharonian et al. 2009b), and 1ES 2344+512 (Acciari et al. 2010). Such a correlation implies that the same high-energy particle population (e.g., electrons) is responsible for the synchrotron emission at X-ray energies, as well as the high-energy IC emission at TeV energies, as predicted in the framework of SSC models. Investigating the exact shape of the X-ray/TeV correlation (linear, quadratic, etc.) will be one of the important goals for future studies. Although this correlation is seen as a general trend, it does not necessarily hold true at the level of individual flares (Krawczynski et al. 2004). In our data, we find indications of an X-ray high state not accompanied by TeV γ-ray flaring (phase 2a) as well as a TeV γ-ray flare without increased X-ray activity (phase 2b). Although the data is not exactly contemporaneous—not allowing for a firm conclusion—such orphan flares in general would require fine tuning of the SSC model (Krawczynski et al. 2004) or alternative models, e.g., external-Compton models or models where the γ-ray emission is produced by hadrons, e.g., as proton-synchrotron emission (Mücke & Protheroe 2001; Aharonian 2002) or through a proton-induced cascade (Mannheim 1998). Further observations are needed to understand this particular aspect of the TeV flaring activity.

Acciari et al. (2009b) reported comparable $\sim$week-scale trends between the Mrk 421 X-ray and optical fluxes without a strong X-ray/TeV coupling. Aharonian et al. (2009a) reported a clear indication of an optical/TeV flux correlation in the case of PKS 2155-304. However, in the second PKS 2155-304 flare the optical/TeV correlation was not seen although the data were again strictly simultaneous (Aharonian et al. 2009b). Also, an optical/TeV correlation is not found in the large data sample presented in this paper or in earlier large data sets. Therefore, it does not seem to be a general property of TeV blazars. This may indicate that (part of) the optical emission is

dominated by a region larger than the TeV emission site and/or a different emission mechanism is at play. However, a certain level of optical synchrotron emission is unavoidable given the synchrotron emission at X-ray energies. The ambiguous findings so far in terms of the optical/TeV correlation may further indicate that different emission scenarios may play a role in different situations, e.g., we do not always observe the same type of flares. No correlation between TeV and radio fluxes has been established at this point resulting in similar arguments as above concerning the emission regions/mechanisms.

TeV flux variations are measured for different TeV blazars with characteristic timescales down to 5–20 minutes (Albert et al. 2007; Aharonian et al. 2009b; Gaidos et al. 1996). Interestingly, the corresponding size of the emission region reaches down to the order of the Schwarzschild radius of the black hole of the corresponding active galactic nucleus (AGN; Albert et al. 2007; Aharonian et al. 2009b). This can be seen as an indication that the TeV γ-ray emission from blazars comes from the base of the jet where the jet energy density is highest and the jet cross-section is smallest. A similar finding was made in the case of the radio galaxy M 87 for which a promising approach to locate the site of the TeV emission region was presented based on the combination of TeV γ-ray observations with simultaneous high-resolution radio observations (Acciari et al. 2009a).

We see two paths toward improving our understanding of the inner workings of AGN jets. The first path involves simultaneous TeV observations with imaging telescopes with $\leqslant$1 mas angular resolution, e.g., Very Long Baseline Array (Acciari et al. 2009a), and/or with polarimetric observations in the optical (Marscher et al. 2008) and the X-ray band.[53] Furthermore, future observations in the MeV/GeV band with *Fermi*, together with observations in the GeV/TeV band with VERITAS, will facilitate the study of the spectral slope, timescales, and correlation of the fluxes in both energy bands which are important inputs for the theoretical modeling. The second path for achieving further progress concerns the theoretical modeling of the results. The analysis presented in this paper confirms that SSC models are successful in describing the broadband SEDs of high-frequency peaked BL Lac (HBL) objects. The two lessons which we infer from the modeling are (1) a large value of the relativistic Doppler factor δ is required to explain the SEDs and the rapid flux variability (Gaidos et al. 1996; Begelman et al. 2008) and (2) in the case of SSC models, the electron energy density exceeds the magnetic field energy density both measured in the rest frame of the emitting volume (see Table 4). In the case of external Compton (EC) models, one can find models with approximately equal electron and magnetic field energy densities (e.g., Ghisellini & Tavecchio 2009), or models in which this ratio deviates considerably from unity (Krawczynski et al. 2002). Considering that protons may add to the particle energy density, the particle energy density may still be an equally comparable component in the plasma blobs producing HBL flares. Further progress can be achieved by combining them with those from theories describing the formation and structure of jets. Recently, general relativistic magnetohydrodynamic simulation codes (e.g., McKinney 2006; Komissarov et al. 2007; Krolik & Hawley 2010; Spruit 2010) have been used to validate aspects of analytic models of the magnetic formation, acceleration, and collimation of jets (Weber & Davis 1967; Blandford & Znajek 1977; Phinney 1983; Camenzind 1986; Lovelace et al. 1987; Li et al. 1992; Vlahakis & Königl 2004; Krawczynski 2007). Giannios et al. (2009) discussed the model of "mini-jets in a jet" driven by magnetic reconnection. Mini-jets in jets may be able to reconcile the predictions of magnetic models of jet formation with the results from SSC (or EC) modeling of the blazar emission of jets: the reconnection mechanism converts magnetic energy into particle energy (Sikora et al. 2005, 2009; Giannios et al. 2009) and may thus be able to explain how particle-dominated plasmas are created in magnetic-field-dominated jets. Furthermore, the creation of mini-jets inside a jet with a modest bulk Lorentz factor can explain jets with very high effective bulk Lorentz factors. This scenario would avoid problems associated with very high bulk Lorentz factors of the jet itself, namely, problems concerning the statistics of detected objects (Henri & Saugé 2006) and concerning tension between high inferred Lorentz factors on the order of 50 and rather slow observed pattern speeds in radio interferometric observations (e.g., Piner et al. 2010). Future work on reconnection might corroborate this possible link between jet formation and the non-thermal emission.

[53] See, for example http://heasarc.gsfc.nasa.gov/docs/gems/.

VERITAS is supported by grants from the U.S. Department of Energy, the U.S. National Science Foundation and the Smithsonian Institution, by NSERC in Canada, by Science Foundation Ireland, and by the STFC in the U.K. We acknowledge the excellent work of the technical support staff at the FLWO and the collaborating institutions in the construction and operation of the instrument. The authors are grateful to the *RXTE* Science Operations Facility and GOF. The Metsähovi team acknowledges the support from the Academy of Finland. The UMRAO is funded by the NSF and the University of Michigan. *Swift*/BAT transient monitor results provided by the *Swift*/BAT team. We also acknowledge *Swift*/XRT monitoring program and target of opportunity support provided by the *Swift* Team and supported by NASA grants NNX08AV77G and NNX08AT31G. We gratefully acknowledge useful discussions with Erik Hoversten regarding *Swift*/UVOT analysis. H.K and A.G. acknowledge support from the NASA grant NNX08AZ76G for the analysis of the *Suzaku* data.

REFERENCES

Abdo, A. A., et al. (Fermi collaboration) 2010, ApJS, 188, 405
Acciari, V. A., et al. (VERITAS collaboration) 2008, ApJ, 679, 1427
Acciari, V. A., et al. 2009a, Science, 325, 444
Acciari, V. A., et al. 2009b, ApJ, 703, 169
Acciari, V. A., et al. (VERITAS collaboration) 2010, ApJ, in press
Aharonian, F. A. 2002, MNRAS, 332, 215
Aharonian, F., et al. (H.E.S.S. & Fermi LAT collaborations) 2009a, ApJ, 696, L150
Aharonian, F., et al. (H.E.S.S. collaboration) 2009b, A&A, 502, 749
Albert, J., et al. (MAGIC collaboration) 2007, ApJ, 669, 862
Albert, J., et al. (MAGIC collaboration) 2008, Science, 320, 1752
Aller, H. D., Aller, M. F., Latimer, G. E., & Hodge, P. E. 1985, ApJS, 59, 513
Arimoto, N. 1996, in ASP Conf. Ser. 98, From Stars to Galaxies: The Impact of Stellar Physics on Galaxy Evolution, ed. C. Leitherer, U. Fritze-von-Alvensleben, & J. Huchra (San Francisco, CA: ASP), 287
Atwood, W. B., et al. 2009, ApJ, 697, 1071
Begelman, M. C., Fabian, A. C., & Rees, M. J. 2008, MNRAS, 384, L19
Berge, D., Funk, S., & Hinton, J. 2007, A&A, 466, 1219
Blandford, R. D., & Znajek, R. L. 1977, MNRAS, 179, 433
Błażejowski, M., et al. 2005, ApJ, 630, 130
Böttcher, M., & Dermer, C. D. 2010, ApJ, 711, 445
Buckley, J. H., et al. 1996, ApJ, 472, L9
Burrows, D. N., et al. 2005, Space Sci. Rev., 120, 165
Camenzind, M. 1986, A&A, 162, 32
de la Calle Perez, I., et al. 2003, ApJ, 599, 909
Edelson, R. A., & Krolik, J. H. 1988, ApJ, 333, 646

Fidelis, V. V., & Iakubovskyi, D. A. 2008, Astron. Rep., 52, 526
Fiorucci, M., & Tosti, G. 1996, A&AS, 116, 403
Fiorucci, M., Tosti, G., & Rizzi, N. 1998, PASP, 110, 105
Fitzpatrick, E. L., & Massa, D. 1999, PASP, 111, 63
Fossati, G., Buckley, J. H., & Bond, I. H. 2008, ApJ, 677, 906
Franceschini, A., Rodighiero, G., & Vaccari, M. 2008, A&A, 487, 837
Fukugita, M., Shimasaku, K., & Ichikawa, T. 1995, PASP, 107, 945
Gaidos, J. A., et al. 1996, Nature, 383, 319
Gao, X., Wang, J., & Yang, J. 2010, Sci. China G: Phys. Astron., 53, 173
Gehrels, N., et al. 2004, ApJ, 611, 1005
Ghisellini, G., & Tavecchio, F. 2009, MNRAS, 397, 985
Giannios, D., Uzdensky, D. A., & Begelman, M. C. 2009, MNRAS, 395, L29
Han, Z., Podsiadlowski, P., & Lynas-Gray, A. E. 2007, MNRAS, 380, 1098
Hartman, R. C., et al. 1999, ApJS, 123, 79
Henri, G., & Saugé, L. 2006, ApJ, 640, 185
Hillas, A. M. 1985, Goddard Space Flight Center 19th Intern. Cosmic Ray Conf., La Jolla, CA
Horan, D., et al. 2009, ApJ, 695, 596
Ishisaki, Y., et al. 2007, PASJ, 59, S113
Jahoda, K., et al. 1996, Proc. SPIE, 2808, 59
Katarzyński, K., & Walczewska, K. 2010, A&A, 510, 63
Kildea, J., et al. 2007, Astropart. Phys., 28, 182
Komissarov, S. S., Barkov, M. V., Vlahakis, N., & Königl, A. 2007, MNRAS, 380, 51
Koyama, K., et al. 2007, PASJ, 59, 23
Krawczynski, H. 2007, ApJ, 659, 1063
Krawczynski, H., Coppi, P. S., & Aharonian, F. 2002, MNRAS, 336, 721
Krawczynski, H., et al. 2000, A&A, 353, 97
Krawczynski, H., et al. 2001, ApJ, 559, 187
Krawczynski, H., et al. 2004, ApJ, 601, 151
Krennrich, F., et al. 2002, ApJ, 575, L9
Krimm, H. 2008a, http://swift.gsfc.nasa.gov/docs/swift/results/transients/
Krimm, H. 2008b, http://swift.gsfc.nasa.gov/docs/swift/results/transients/Transientsynopsis.html
Krolik, J. H., & Hawley, J. F. 2010, in The Jet Paradigm (Lecture Notes in Physics, Vol. 794; Berlin: Springer), 265
Levine, A. M., Bradt, H., Cui, W., Jernigan, J. G., Morgan, E. H., Remillard, R., Shirley, R. E., & Smith, D. A. 1996, ApJ, 469, L33
Li, T., & Ma, Y. 1983, ApJ, 272, 317
Li, W., Jha, S., Filippenko, A. V., Bloom, J. S., Pooley, D., Foley, R. J., & Perley, D. A. 2006, PASP, 118, 37
Li, Z.-Y., Chiueh, T., & Begelman, M. C. 1992, ApJ, 394, 459
Lichti, G. G., et al. 2008, A&A, 486, 721
Lockman, F. J., & Savage, B. D. 1995, ApJS, 97, 1
Lovelace, R. V. E., Wang, J. C. L., & Sulkanen, M. E. 1987, ApJ, 315, 504
Mannheim, K. 1998, Science, 279, 684
Marscher, A. P., et al. 2008, Nature, 452, 966
Massaro, E., Perri, M., Giommi, P., & Nesci, R. 2004, A&A, 413, 489
Massaro, E., Tramacere, A., Perri, M., Giommi, P., & Tosti, G. 2006, A&A, 448, 861
McKinney, J. C. 2006, MNRAS, 368, 1561
Mitsuda, K., et al. 2007, PASJ, 59, S1
Mücke, A., & Protheroe, R. J. 2001, Astropart. Phys., 15, 121
Nilsson, K., Pursimo, T., Takalo, L. O., Sillanpää, A., Pietilä, H., & Heidt, J. 1999, PASP, 111, 1223
Phinney, E. S. 1983, PhD thesis, Univ. Cambridge
Piner, B. G., Pant, N., & Edwards, P. G. 2010, ApJ, 723, 1150
Poole, T. S., et al. 2008, MNRAS, 383, 627
Punch, M., & Fegan, D. J. 1991, in AIP Conf. Proc. 220, High Energy Gamma Ray Astronomy, ed. J. Matthews (Melville, NY: AIP), 321
Punch, M., et al. 1992, Nature, 358, 477
Rebillot, P. F., et al. 2006, ApJ, 641, 740
Reynolds, P. T., et al. 1993, ApJ, 404, 206
Rieger, F. M. 2004, ApJ, 615, L5
Rothschild, R. E., et al. 1998, ApJ, 496, 538
Schlegel, D. J., Finkbeiner, D. P., & Davis, M. 1998, ApJ, 500, 525
Sikora, M., Begelman, M. C., Madejski, G. M., & Lasota, J.-P. 2005, ApJ, 625, 72
Sikora, M., Stawarz, L., Moderski, R., Nalewajko, K., & Madejski, G. M. 2009, ApJ, 704, 38
Snellen, I. A. G., McMahon, R. G., Hook, I. M., & Browne, I. W. A. 2002, MNRAS, 329, 700
Spruit, H. C. 2010, in The Jet Paradigm (Lecture Notes in Physics, Vol. 794; Berlin: Springer), 233
Stecker, F. W., Baring, M. G., & Summerlin, E. J. 2007, ApJ, 667, L29
Steele, D., et al. 2008, in Proc. 30th International Cosmic Ray Conference, Merida, Yucatan, ed. R. Caballero et al., Univ Nacional Autonoma de Mexico, 3, 989 (arXiv:0709.3869)
Swank, J. H. 1994, American Astronomical Society Meeting, 185, 6701 (BAAS, 26, 4)
Tammi, J., & Duffy, P. 2009, MNRAS, 393, 1063
Teräsranta, H., et al. 1998, A&AS, 132, 305
Villata, M., Raiteri, C. M., Lanteri, L., Sobrito, G., & Cavallone, M. 1998, A&AS, 130, 305
Vlahakis, N., & Königl, A. 2004, ApJ, 605, 656
Wakely, S., & Horan, D. 2010, TeV Cat, http://tevcat.uchicago.edu/
Weber, E. J., & Davis, L., Jr. 1967, ApJ, 148, 217
Weekes, T. C. 1996, Space Sci. Rev., 75, 1